Multistep Redox Systems, LXVIII[+]

Violene/Cyanine Hybrids as Electrochromics Part 2: Tetrakis(4-dimethylaminophenyl)ethene and Its Derivatives**

Siegfried Hünig,*[a] Martina Kemmer,[a] Hermann Wenner,[a] Frédérique Barbosa,[b] Georg Gescheidt,[b] Igor F. Perepichka,[c] Peter Bäuerle,[d] Andreas Emge,[d] and Karl Peters[e]

Abstract: The general structure of violene/cyanine hybrids (see below) is exemplified by tetrakis(4-dimethylaminophenyl)ethene $\mathbf{1}_{RED}$ its vinylogue $\mathbf{2}_{RED}$ and its diazavinylogue $\mathbf{3}_{RED}$. As judged from their cyclic voltammograms and spectroelectrograms, oxidation occurs perfectly reversible by loss of two electrons creating closed shell systems $\mathbf{1}-\mathbf{3}_{OX}{}^{+2}$ with strong bathochromic shifts (Michlers hydrol blue moieties). ESR spectra indicate only minor amounts of radical cations. At much higher potentials by another reversible loss of two electrons ($\rightarrow \mathbf{1}-\mathbf{3}_{OX}{}^{+4}$) the long wavelengths absorptions are replaced by shorter ones. In system **4**, containing two 4-dimethylaminophenyl units only, the violene character is better preserved since oxidation occurs stepwise by single electron transfer up to $\mathbf{4}_{OX}{}^{+4}$. These results are backed by theoretical calculations for **1**–**4**, demonstrating the strong geometrical differences between the various oxidation levels. Besides, new types of cyclic structures for $\mathbf{1}-\mathbf{4}_{OX}{}^{+4}$ are indicated by these calculations: For systems **1**–**3** cyclic structures for tetracations have been found to be more stable by 3–20 kcal mol^{-1} than acyclic structures, whereas for system **4** the acyclic structure is more stable by about 22 kcal mol^{-1}. The redox behavior of systems **1**–**4** is of general importance for electrochromic systems.

Keywords: cyanines · electrochromics · electrochemistry · theoretical calculations · violenes

Introduction

Recently, in this journal, we have proposed the general structure **A** (see below) for electrochromic systems.[2] It allows for reversible electron transfer due to its "violene" type character,[4] but contains the moieties X-C-Y as end groups, which represent at least one "cyanine" type structure in the fully reduced or oxidized form; this provides highly colored *closed* shell systems by an overall two-electron transfer.

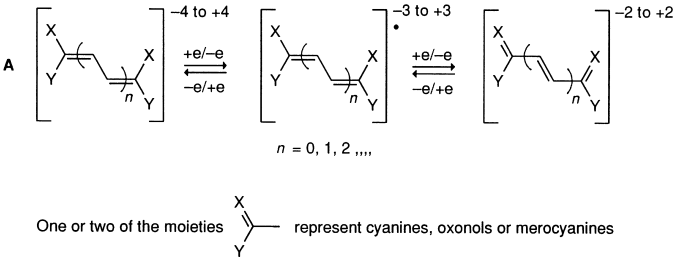

As typical examples we now present details on the redox systems tetrakis(4-dimethylaminophenyl)ethene ($\mathbf{1}_{RED}$)[2] and the closely related compounds $\mathbf{2}_{RED}$,[2] $\mathbf{3}_{RED}$, and $\mathbf{4}_{RED}$.[2]

Results and Discussion

System 1

As early as 1906 $\mathbf{1}_{RED}$ was described[5] and later chemically oxidized to its dication $\mathbf{1}_{OX}{}^{+2}$ which was isolated at its

[a] Prof. S. Hünig, M. Kemmer, H. Wenner
Institut für Organische Chemie der Universität Würzburg
Am Hubland, 97074 Würzburg (Germany)
Fax: (+49) 931 8884606
E-mail: huenig@chemie.uni-wuerzburg.de

[b] Dr. F. Barbosa, Prof. G. Gescheidt
Institut für Physikalische Chemie der Universität Basel
Klingelbergstrasse 80, 4056 Basel (Switzerland)

[c] Dr. I. F. Perepichka
L.M. Litvinenko Institute of Physical Organic and Coal Chemistry, National Academy of Sciences of Ukraine
R. Luxemburg Street 70, Donetsk 340114 (Ukraine)

[d] Prof. P. Bäuerle, Dr. A. Emge
Organische Chemie II, Universität Ulm
Albert-Einstein-Allee 11, 89081 Ulm (Germany)

[e] Prof. K. Peters
MPI für Festkörperforschung
Heisenbergstrasse 1, 70506 Stuttgart (Germany)

[**] For part 1: see ref. [2]

[+] Part LXVII: see ref. [1]

  0947-6539/00/0614-2618 $ 17.50+.50/0

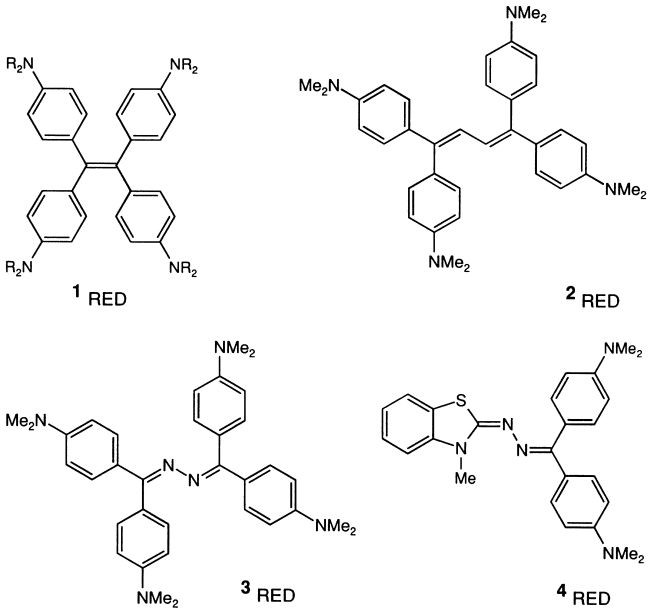

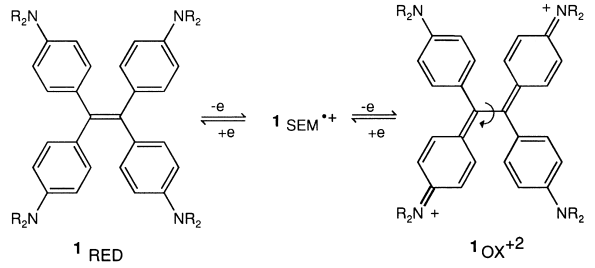

Scheme 1. Redox system **1**.

diperchlorate[6a] and bis(triiodide).[6b] We prepared $\mathbf{1_{OX}}^{+2}\cdot 2BF_4^-$ in analogy to the reference.[6a]

Electrochemistry, ESR, ENDOR, and SEOS (simultaneous optical and ESR spectra): Due to its inherent violene type system **1** is supposed to behave as a two step redox system according to Scheme 1.

At first glance the cyclic voltammogram (CV) of **1** seems to confirm this assumption since two strongly separated reversible oxidation steps are observed (Figure 1). On a closer look, however, the potential $E_{1/2}{}^1 = 303$ mV ($E_{pa}{}^1 - E_{pc}{}^1 = 34$ mV) corresponds already to the transfer of two electrons, that is $\mathbf{1_{RED}} \rightarrow \mathbf{1_{OX}}^{+2}$ (Figure 1, Table 1). Indeed, a thorough electrochemical study by A. J. Bard[7] already revealed an overall

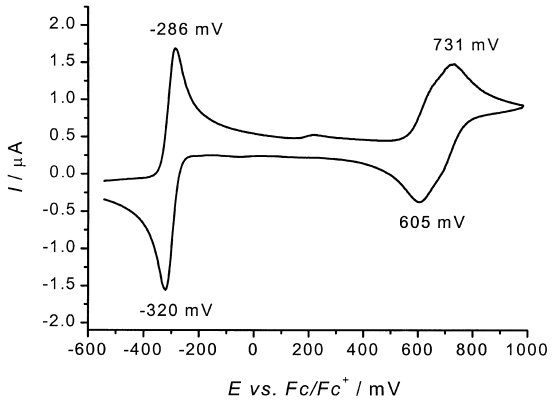

Figure 1. Cyclic voltamogram of $\mathbf{1_{RED}}$ in $CH_2Cl_2/n\text{-}Bu_4N^+PF_6^-$ (0.1M) versus Fc/Fc^+. Scan rate 100 mV s^{-1}.

two-electron transfer in which the second electron is abstracted at somewhat *lower* potentials than the first. This behavior depends mainly on the strong donor -NMe_2 ($\sigma_p = -0.63$) since its replacement by -OMe ($\sigma_p = -0.28$) in tetrakis(4-methoxyphenyl)ethene (TME) produces a normal two step redox system with closely placed potentials E_1 and E_2.[7] In dichloromethane the semiquinone formation constant K of TME was calculated to 55 whereas in acetonitrile it dropped to 1.5, since this dipolar solvent stabilizes higher charged species more than dichloromethane. Consequently, the radical cation of TME can be easily identified by ESR in dichloromethane.[7] For $\mathbf{1_{SEM}}^{\bullet+}$ Bard calculated an equilibrium concentration of about 3% in dichloromethane (not 20% as stated in ref.[6b]) characterized by an unresolved ESR signal.

Now, after some experimentation, conditions for resolved ESR spectra of $\mathbf{1_{SEM}}^{\bullet+}$ were found. After oxidation of donor **1** with $AgClO_4$, tris(*p*-bromophenyl)ammoniumyl hexachloroantimonate, or thallium(III)trifluoroacetate in CH_2Cl_2 well-resolved ESR spectra could be recorded (Figure 2). A corresponding ENDOR spectrum indicates proton hyperfine coupling constants, ^1H hfcs, of 0.143, 0.066, and 0.019 mT. The simulation of the ESR signal reveals that the ^1H hfcs are due to 24, 8, and 8 equivalent protons, respectively; moreover, a ^{14}N hfc of 0.152 mT (4 equiv N) has to be included to achieve

Abstract in German: *Die allgemeine Struktur der Violen/Cyanin Hybride (siehe unten) wird durch die Beispiele Tetrakis(-4-dimethylaminophenyl)ethen (**1**$_{RED}$), seinem Vinylogen **2**$_{RED}$ sowie seinem Diazavinylogen **3**$_{RED}$ illustriert. Aufgrund ihrer Cyclovoltamogramme und Spektroelektrogramme verläuft die Oxidation völlig reversibel unter Verlust von zwei Elektronen. Dabei entstehen die closed-shell-Systeme **1**–**3**$_{OX}^{+2}$ mit stark bathochromer Absorption (Michlers Hydrolblau Typ). ESR-Spektren lassen nur minimale Konzentrationen an Radikalkationen erkennen. Bei wesentlich höheren Potentialen tritt ein weiterer reversibler Zweielektronenübergang auf (→**1**–**3**$_{OX}^{+4}$), wobei die langwelligen Absorptionen durch kürzerwellige ersetzt werden. Im System **4**, das nur zwei 4-Dimethylaminophenyl-Einheiten enthält, tritt der Violencharakter stärker hervor, denn die Oxidation erfolgt in einzelnen Stufen bis **4**$_{OX}^{+4}$. Diese Ergebnisse werden für **1**–**4** durch theoretische Berechnungen gestützt, welche die starken geometrischen Unterschiede zwischen den einzelnen Oxidationsstufen zeigen. Außerdem wurden für **1**–**4**$_{OX}^{+4}$ neue cyclische Strukturen berechnet. Dabei zeigt sich, daß diese cyclischen Tetrakationen für die Systeme **1**–**3** um 3–20 kcal mol^{-1} energiereicher sind, als die offenkettigen, während im Falle von **4**$^{+4}$ die cyclische Struktur um ca. 22 kcal mol^{-1} energieärmer ist. Das Redoxverhalten der Systeme **1**–**4** ist für elektrochrome Systeme von allgemeiner Bedeutung.*

Table 1. Peak potentials (mV vs. Fc^0/Fc^+) E_{pa} and E_{pc} determined by cyclic voltammetry in CH_2Cl_2/n-$Bu_4N^+PF_6^-$ (0.1M) at scan rate 100 mV s^{-1}, calculated redox potentials $E_{1/2}{}^1$ and $E_{1/2}{}^2$, and their differences $\Delta E_{1/2}{}^{1-2}$.

System[a]	$E_{pa}{}^1$	$E_{pc}{}^1$	$E_{1/2}{}^1$	$E_{pa}{}^2$	$E_{pc}{}^2$	$E_{1/2}{}^2$	$\Delta E_{1/2}{}^{1-2}$
1	−286	−320	−303[b]	731	605	0.634,[c,d] 0.701[c,d]	0.937, 1.004
2	−156	−221	−188[b]	760	705	732[b]	920
3	195	138	166[b]	720	627	673[b]	507
4	105	31	68[c]	320	248	284[c]	216

[a] Initial states of all the compounds in CV experiments were their reduced forms ($\mathbf{1}_{RED}-\mathbf{4}_{RED}$); [b] two-electron transfer; [c] single electron transfer; [d] calculated values based on supposition of the electrochemically reversible process (see explanations in the text).

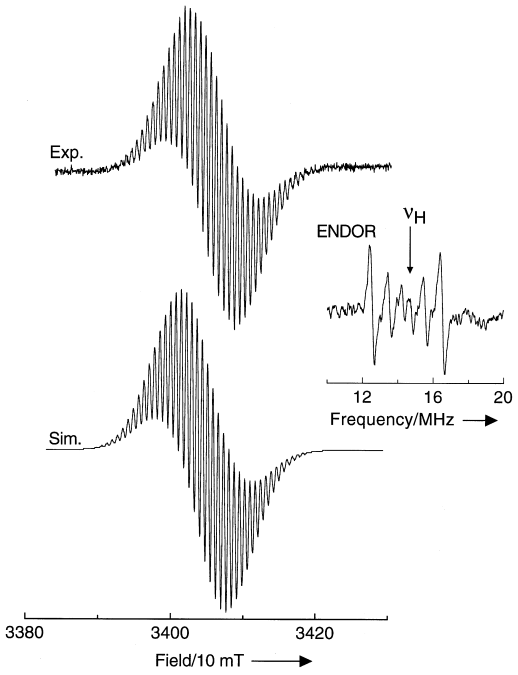

Figure 2. ESR spectrum of $\mathbf{1}_{SEM}{}^{\bullet+}$ and its simulation together with its ENDOR spectrum.

the fit with the experimental ESR spectrum (Figure 2). Accordingly the spin and the charge are delocalized in the entire π system of $\mathbf{1}^{\bullet+}$.

Figure 3 presents the geometry of $\mathbf{1}_{SEM}{}^{\bullet+}$ from ab initio calculations (UHF/3-21G* level of theory). With respect to the length of the central bond and the four equivalent torsions angles ω of the aromatic substituents the data nearly duplicate those of PM3 calculations (Table 2). Experimental and calculated spin densities are in good agreement with highest densities at the nitrogen atoms (see Computational procedures).

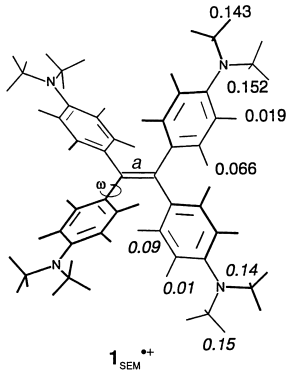

Figure 3. Experimental (displayed in the upper right moieties) and calculated (UB3LYP/6–31G*//UHF/3–21G*, in italics; displayed in the lower right moieties) hfcs determined for $\mathbf{1}_{SEM}{}^{\bullet+}$: $a = 142.7$ pm, $\omega = 35.5°$.

Immediately after the oxidation the originally yellow solution turns green but changes to violet within a few minutes (independent of the oxidant). In parallel, the intensity of the ESR spectra rises. Electronic absorption spectra taken simultaneously with ESR signals[8] (SEOS) are virtually identical to the absorption spectrum ascribed to $\mathbf{1}^{+2}$ in Figure 4. The perception that the absorption bands with λ_{max} at 478, 538, and 750 nm increase parallel to the ESR intensities points to the radical cation having long-wave absorption bands in the same region as the dication. However, an assignment of specific bands to the radical cation is not attainable because of the superimposed absorptions of $\mathbf{1}^{\bullet+}$ and $\mathbf{1}^{+2}$.

This conclusion is confirmed by the spectroelectrogram of Figure 4 which produces exactly the UV/Vis spectra of $\mathbf{1}_{RED}$

Table 2. Parameters of PM3-optimized structures for system **1** at different oxidation levels and selected data for $\mathbf{1}_{RED}$ from single crystal X-ray determination.[a]

	$\mathbf{1}_{RED}$	$\mathbf{1}_{RED}$ (X-ray)	$\mathbf{1}_{SEM}{}^{\bullet+}$	$\mathbf{1}_{OX}{}^{2+}$	$\mathbf{1}_{SEM}{}^{\bullet 3+}$	$\mathbf{1}_{OX}{}^{4+}$(A)	$\mathbf{1}_{OX}{}^{4+}$(C)
Total energy [hartree]	−194.49855		−194.24642	−193.91615	−193.52678	−192.92112	−192.95364
Heat of formation [kcal mol^{-1}]	104.78		262.99	470.24	714.58	1094.64	1074.24
HOMO [eV]	−8.18			−12.61		−16.90	−18.45
SOMO [eV]	−10.00 (α)[b]		−13.96				
		−0.30 (β)[b]		−14.13			
LUMO [eV]	0.39		−4.25 (α)	−7.35	−9.39	−14.40	−12.48
		−5.56 (β)		−9.79			
Dipole moment [Debye]	0.24		14.25	0.00	16.49	0.02	1.38
d (C2–C1) [pm]	134.5	137.0(7)	142.6	150.4	145.8	150.7	147.0
α (C9-C2-C1-C3) [°]	0.0	10.8	33.8	80.6	52.8	83.4	23.7
γ_A (C20-C15-C2-C1) [°]	86.9	49.4	19.3	15.2	22.6	16.4	3.0
γ_B (C22-C21-C1-C2) [°]	86.7	48.4	46.9	15.2	40.6	16.4	3.2
γ_C (C8-C3-C1-C2) [°]	87.0	54.6	30.1	15.2	20.8	15.3	49.2
γ_D (C10-C9-C2-C1) [°]	86.9	42.9	52.0	15.2	34.7	15.3	49.2

[a] Attribution of a bond distance d and torsion angles α, and $\gamma_A-\gamma_D$ see in Figures 6 and 7 . Signs of rotations for torsion angles are omitted; [b] orbital energies for α and β electrons.

0947-6539/00/0614-2620 $ 17.50+.50/0 *Chem. Eur. J.* **2000**, *6*, No. 14

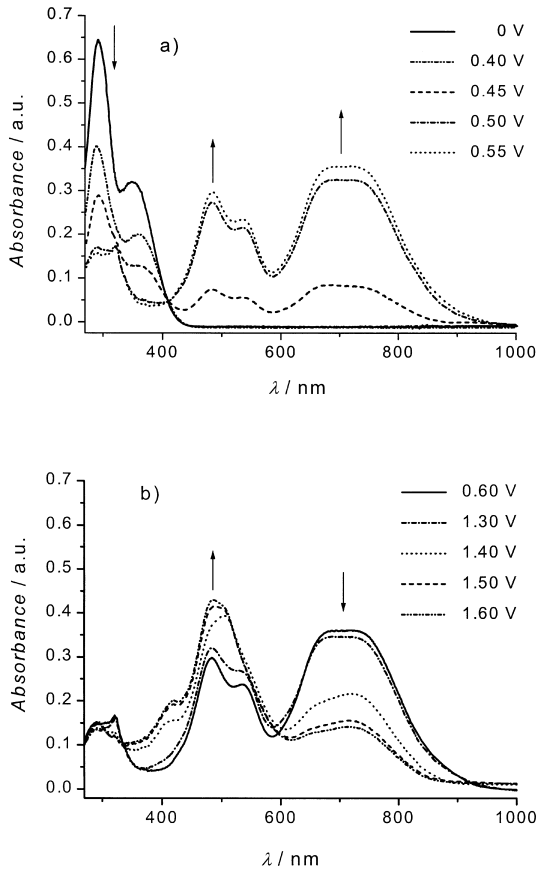

Figure 4. Spectroelectrogram of **1** on stepwise oxidation (CH_3CN, 0.1 M n-$Bu_4N^+PF_6^-$, potentials are given versus Ag/AgCl): a) $\mathbf{1}_{RED} \rightarrow \mathbf{1}_{OX}^{+2}$; b) $\mathbf{1}_{OX}^{+2} \rightarrow \mathbf{1}_{OX}^{+4}$.

and $\mathbf{1}_{OX}^{+2}$, respectively. The excellent isosbestic point leaves no room for substantial amounts of $\mathbf{1}_{SEM}^{\bullet+}$. Accordingly, the UV/Vis spectrum of $\mathbf{1}_{OX}^{+2}$ is not changed on addition of $\mathbf{1}_{RED}$.

System **1** provides an extremely strong shift in color from $\mathbf{1}_{RED}$ ($\lambda_{max} = 295$, 355 nm, colorless) to $\mathbf{1}_{OX}^{+2}$ ($\lambda_{max} = 490$, 540, ca. 690–750 nm). The longest and very broad wavelength absorption is obviously caused by two separate bands of nearly identical intensity, similar to the two bands at shorter wavelengths. Since $\mathbf{1}_{OX}^{+2}$ can be envisaged as composed from two moieties of Michlers hydrol blue with a narrow absorption band at 614 nm (log $\varepsilon = 5.18$, CH_2Cl_2)[9] such a complicated pattern of absorbance was not expected. The bathochromic shift may be explained to the extra positive charge at the central carbon atoms, similar to the effect of the central nitrogen in Bindschedlers green ($\lambda_{max} = 725$ nm).[10]

This way, in system **1** the colored form constitutes a closed shell system, in contrast to those of violene systems (e.g. the radical cation derived from 4,4′-dipyridinium salts or Wursters Blue) and surpasses the latter both by its longer wavelength shift and stronger absorption.[4c]

The next redox peaks which appear at a more positive potential of about +0.7 V can be attributed also to a two-electron transfer $\mathbf{1}_{OX}^{+2} \rightarrow \mathbf{1}_{OX}^{+4}$. However, as seen from Figure 1, these peaks are somewhat broadened with shoulders before E_{pa}^{2} and E_{pc}^{2} (although their integral intensities, as compared with E_{pa}^{1} and E_{pc}^{1}, also correspond to an overall two-electron process). This can be explained by very closely spaced single-electron transfers [$\mathbf{1}_{OX}^{+2} - e \rightarrow \mathbf{1}_{SEM}^{\bullet+3}$ (E^{2a}) and $\mathbf{1}_{SEM}^{\bullet+3} - e \rightarrow \mathbf{1}_{SEM}^{+4}$ (E^{2b})] due to low thermodynamic stability of $\mathbf{1}_{SEM}^{\bullet+3}$. Both E^{2a} and E^{2b} values can be estimated assuming an electrochemically reversible process with $E_{pa} - E_{pc} = 59$ mV. This way the potentials of both shoulders can be calculated from the peak potentials according to $E_{pa}^{2a} = E_{pc}^{2a} + 59 = 664$ mV and $E_{pc}^{2b} = E_{pa}^{2} - 59 = 672$ mV. From these two closely spaced values the corresponding $E_{1/2}$ potentials can be derived as $E_{1/2}^{2a} = (E_{pa}^{2a} + E_{pc}^{2a})/2 = 634$ mV and $E_{1/2}^{2b} = (E_{pa}^{2b} + E_{pc}^{2b})/2 = 701$ mV; this indicates the formation of $\mathbf{1}_{SEM}^{\bullet+3}$ and $\mathbf{1}_{OX}^{+4}$, respectively.

PM3 calculations and X-ray molecular structure: In order to ascertain how the oxidation of $\mathbf{1}_{RED}$ changes the geometry of the molecule we carried out a series of calculations of the structures $\mathbf{1}_{RED} - \mathbf{1}_{OX}^{+4}$ with full optimization of the geometry by the MNDO-PM3 semiempirical method. From these calculations (Table 2) the following lowest energy conformations at the different oxidation levels $\mathbf{1}_{RED}$ to $\mathbf{1}_{OX}^{+4}$ are derived (Figure 5). For comparison the X-ray structure for $\mathbf{1}_{RED}$ has been included (Figure 6). One should keep in mind that with

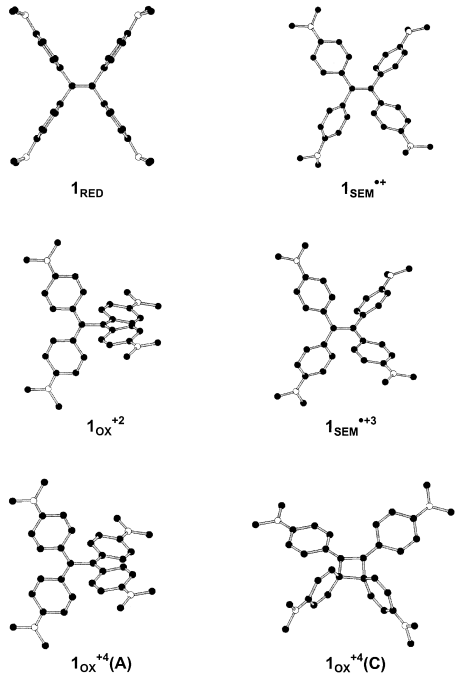

Figure 5. PM3-optimized geometries of compound **1** at various oxidation states (hydrogen atoms are omitted; closed circles are carbon atoms, open circles are nitrogen atoms).

$E_{1/2}^{1} = -303$ mV, system **1** is rather easily oxidized and the dramatically more positive $E_{1/2}^{2a} = 634$ mV, $E_{1/2}^{2b} = 701$ mV represent higher oxidation levels from which still reversible reduction occurs. Therefore structures for $SEM^{\bullet+3}$ and OX^{+4} states have been calculated as well. For discussion we enumerated clockwise four phenyl rings in **1**, from **A** to **D**, as shown in Figure 7.

As can be seen from Figure 3 and Table 2, these species differ remarkably with respect to the torsion angle at the central C–C bond (α) and torsion angles between the phenyl rings and central C–C bonds (γ_A, γ_B, γ_C, and γ_D, (see above).

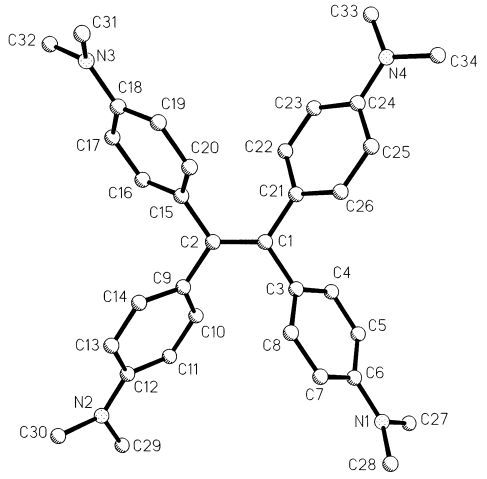

Figure 6. Single crystal X-ray molecular structure of $\mathbf{1}_{\mathbf{RED}}$.

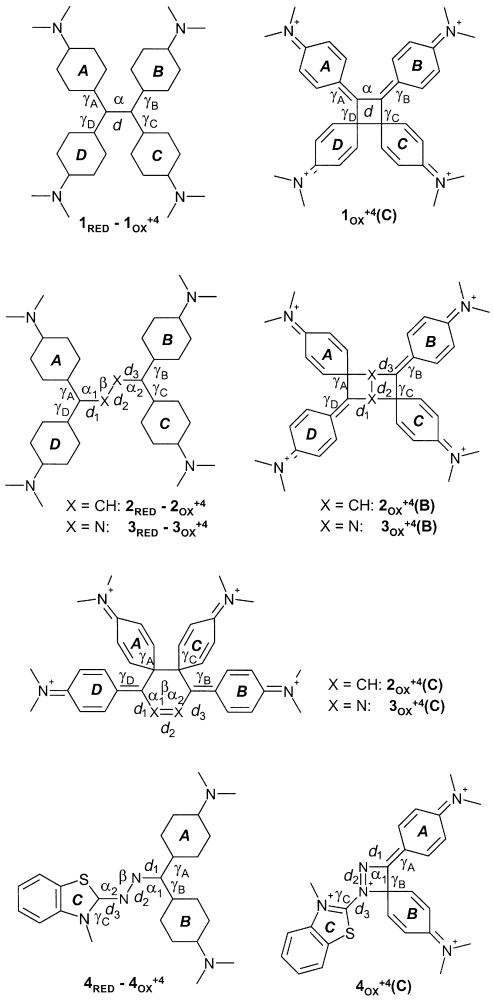

Figure 7. Bond distances (d), and torsion angles (α, β, and γ) in systems **1–4** (for the PM3 calculated values see Tables 2–5). Charges on nitrogens and double bonds for $\mathbf{1}_{\mathbf{RED}}$–$\mathbf{1}_{\mathbf{OX}}{}^{+4}$, $\mathbf{2}_{\mathbf{RED}}$–$\mathbf{2}_{\mathbf{OX}}{}^{+4}$, $\mathbf{3}_{\mathbf{RED}}$–$\mathbf{3}_{\mathbf{OX}}{}^{+4}$, and $\mathbf{4}_{\mathbf{RED}}$–$\mathbf{4}_{\mathbf{OX}}{}^{+4}$ are omitted.

As expected, the central double bond in $\mathbf{1}_{\mathbf{RED}}$ is practically planar with all four attached C–C bonds (torsion angle $\alpha = 0.0^\circ$) whereas the four aromatic rings are twisted out of plane nearly perpendicularly ($\gamma_A - \gamma_D \approx 87^\circ$). Interestingly, the crystal structure of $\mathbf{1}_{\mathbf{RED}}$ shows a definitely stronger twisted C=C bond (11°) and consequently less twisted aromatic groups (43–55°). These differences may well be due to crystal packing and also, partly, due to underestimating the conjugation of phenyl rings with the central C=C bond by the PM3 method. It should be, however, mentioned that the cost of energy for moving from the PM3 optimized structure of $\mathbf{1}_{\mathbf{RED}}$ (Figure 5) to structures with decreased torsion angles γ is rather small: Thus, a local minimum of only 3.2 kcal mol^{-1} higher energy was found with torsion angles $\gamma_A - \gamma_D$ of 60–70° (α remains 0°).

Interestingly, removal of one electron from $\mathbf{1}_{\mathbf{RED}}$ causes a remarkably stronger torsion angle α of the central C=C bond in the resulting radical cation $\mathbf{1}_{\mathbf{SEM}}{}^{\bullet+}$ ($\alpha = 34^\circ$) together with a somewhat (+8 pm) stretched central bond. Such a twisting leads, on the other hand, to the possibilities of less twisted phenyl rings ($\gamma_A \cdots \gamma_D \approx 19–52^\circ$). These PM3 results are backed by the above-mentioned structure of $\mathbf{1}_{\mathbf{SEM}}{}^{\bullet+}$ derived from ESR measurements and ab initio calculations (Figure 3).

An extrusion of another electron to $\mathbf{1}_{\mathbf{OX}}{}^{+2}$ causes dramatic alterations of the structure. The central bond becomes practically a single one (150 pm) and the two only slightly twisted ($\gamma_A = \gamma_B = \gamma_C = \gamma_D = 15^\circ$) Michlers hydrol blue moieties are found nearly perpendicular to one another ($\alpha = 81^\circ$). The high driving force to $\mathbf{1}_{\mathbf{OX}}{}^{+2}$ may be at least partly due to relief of strain. Similar geometries were already calculated for $\mathbf{5}_{\mathbf{OX}}{}^{+2}$ the oxidation product of tetrakis(dimethylamino)ethene (see below, angles [N_2C–CN_2] 76° (dichloride) and 67° (dibromide)).[11]

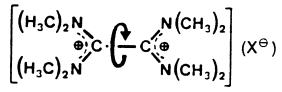

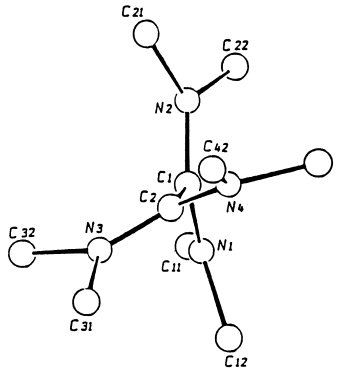

Nevertheless, mainly electronic factors must be responsible for the twisted structure which is already found for ethene on oxidation to its dication.[12] As can be seen from Figure 5 and Table 2, the geometries [bond lengths (d) and torsion angles (α and $\gamma_A - \gamma_D$)] of SEM$^{\bullet+3}$ and OX^{+4}(A) resemble very close those of SEM$^{\bullet+1}$ and OX^{+2}, respectively. A similar situation is also observed for charge delocalization: $\mathbf{1}_{\mathbf{RED}}$, $\mathbf{1}_{\mathbf{OX}}{}^{+2}$, and $\mathbf{1}_{\mathbf{OX}}{}^{+4}$**(A)** are almost symmetrical with no resulting dipole moment for the molecules, whereas $\mathbf{1}_{\mathbf{SEM}}{}^{\bullet+}$ and $\mathbf{1}_{\mathbf{SEM}}{}^{\bullet+3}$ show substantial dipole moments (14.3 and 16.5 D, respectively; Table 2).

It is important to note that comparison of two structures for tetracation, that is acyclic $\mathbf{1}_{\mathbf{OX}}{}^{+4}$**(A)** and cyclic $\mathbf{1}_{\mathbf{OX}}{}^{+4}$**(C)** shows the latter to be more stable: If OX^{+4} (A) is cyclized to the corresponding cyclobutane OX^{4+}(C), 20.40 kcal mol^{-1} are

  0947-6539/00/0614-2622 $ 17.50+.50/0 *Chem. Eur. J.* **2000**, *6*, No. 14

gained in energy. We therefore suggest this cyclic structure for the totally oxidized system **1**.

System 2

This systems constitutes the vinylogue of **1**. It was chosen to study the effects of lesser steric congestion and larger distances of the developing charges on oxidation.

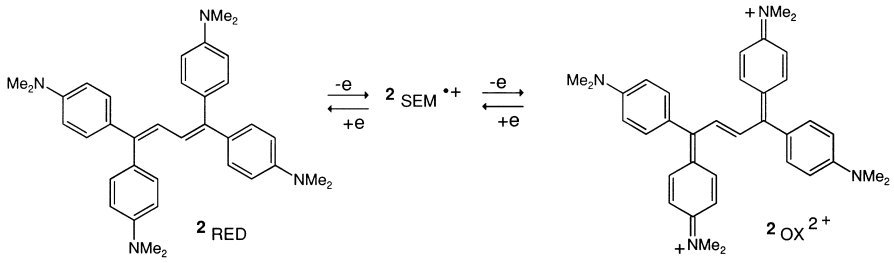

Scheme 3. Redox system **3**.

Synthesis: The vinylogue of **1**, 1,1,4,4-tetrakis(4-dimethylaminophenyl)-1,3-butadiene ($\mathbf{2_{RED}}$), has been briefly mentioned as a minor product (13% yield) from the treatment of 1,1-bis(4-dimethylaminophenyl)ethene (**6**) with bromine.[13] We easily obtained $\mathbf{2_{RED}}$ in pure state with a good yield (70%) as pale yellow solid according to Scheme 2.

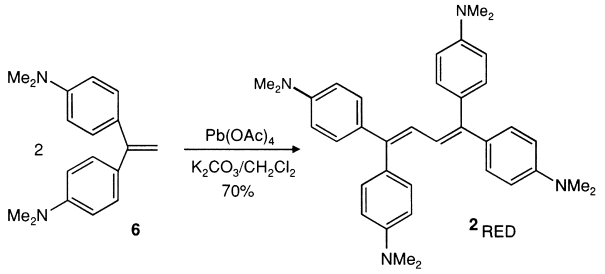

Scheme 2. Synthesis of $\mathbf{2_{RED}}$.

Electrochemistry, ESR and ENDOR: The CV of $\mathbf{2_{RED}}$ again consists of two reversible redox steps (Figure 8). However, the CH–CH bridge decreases the donor properties of the system resulting in a positive shift of oxidation potential $E_{1/2}{}^1$ of $\mathbf{2_{RED}}$ as compared with $\mathbf{1_{RED}}$. Due to less Coulomb repulsion in **2**

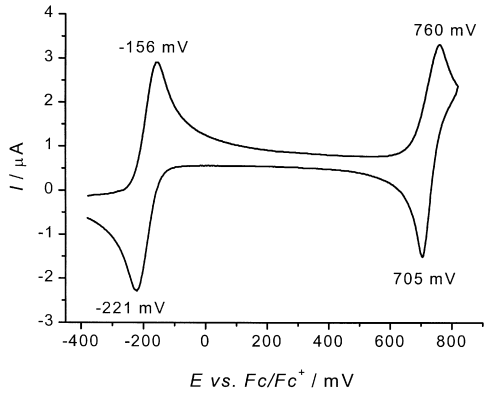

Figure 8. Cyclic voltammogram of $\mathbf{2_{RED}}$ in CH_2Cl_2/*n*-$Bu_4N^+PF_6^-$ (0.1M) versus Fc/Fc^+. Scan rate 100 mV s^{-1}.

compared with **1** the difference in potentials ($\Delta E_{1/2}{}^{1-2} = E_{1/2}{}^2 - E_{1/2}{}^1$) somewhat shrinks (Table 1). If a stepwise transfer of two electrons (Scheme 3) is hidden in $E_{1/2}{}^2$ of **2** the potentials must be closer than in $E_{1/2}{}^2$ of **1** according to the much slender curves. On slight oxidation, according to $\mathbf{1_{RED}}$, again only traces of $\mathbf{2_{SEM}}^{\bullet+}$ were observed (Figure 10). Combined data

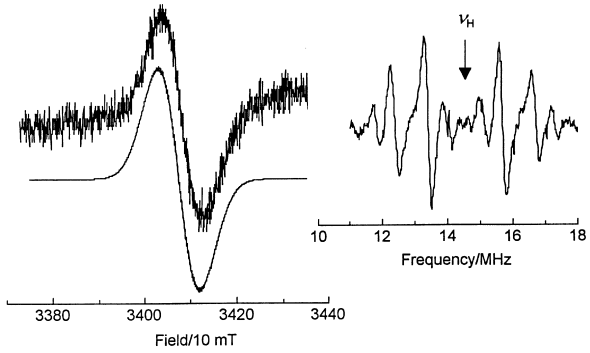

Figure 9. ESR spectrum of $\mathbf{2_{SEM}}^{\bullet+}$ and its simulation together with its ENDOR spectrum.

from the unresolved ESR spectrum and the ENDOR spectrum allowed assignments of the spin densities as shown in Figure 10 in good agreement with those from ab initio calculations (at UB3LYP/6-31G*//UHF:3-21G* level of theory; see Computational procedures).

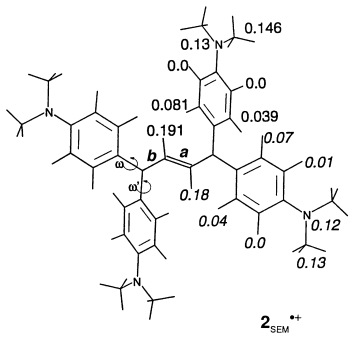

Figure 10. Experimental (displayed in the upper right moieties) and calculated (UB3LYP/6–31G*//UHF/3–21G*, in italics; displayed in the lower right moieties) hfcs determined for $\mathbf{2_{SEM}}^{\bullet+}$: $a = 138.2$ pm, $b = 129.0$ pm, $\omega = 21.7°$, $\omega' = 52.8°$.

In the radical cation of $\mathbf{2_{SEM}}^{\bullet+}$, the predominate spin population resides in the central C-CH=CH-C moiety but also a considerable amount is delocalized into the 4-dimethylaminophenyl substituents. This is borne out by the ^{14}N hfcs of 0.13 mT and the ^1H hfcs of 0.146 mT attributed to the two *N*-methyl substituents. According to the calculations, the four dimethylaminophenyl groups are only pairwise equivalent; however, the ESR data indicate that the conformations of the aryl substituents are equilibrated on the ESR hyperfine time scale (ca. 10^{-9} s). Therefore the calculated hfcs indicated in

Figure 10 represent averaged values from the two differently twisted dimethylaminophenyl substituents.

The calculated bond lengths *a* and *b* together with the torsion angles ω and ω' (Figure 10) compare rather well to those from PM3 evaluations (Table 3) but stronger differences are found in the bond lengths of the C_4 backbone. The differences in the torsion angles should not be overestimated due to the high flexibility of the shown conformation of $\mathbf{2_{SEM}}^{\bullet+}$.

Due to the very low concentration of $\mathbf{2_{SEM}}^{\bullet+}$, potentials $E_{1/2}{}^1 = -188$ mV and $E_{1/2}{}^2 = 732$ mV correspond to the transfer of two electrons in both cases. The spectroelectrogram of $\mathbf{2_{RED}}$ (Figure 11a–b) therefore can be interpreted as follows. In Figure 11a the isosbestic point at about 430 nm signalizes a redox equilibrium between two species only, namely the decreasing concentration of $\mathbf{2_{RED}}$ (↓355 nm, ↓400 nm) and the formation of $\mathbf{2_{OX}}^{2+}$ (↑465 nm, ↑750 nm) according to Scheme 3. Further increasing potentials (Figure 11b) produce a new species [↑545 nm (shoulder), ↑590 nm] probably caused by $\mathbf{2_{OX}}^{4+}$ at the cost of $\mathbf{2_{OX}}^{2+}$ (↓465 nm, ↓770 nm). This equilibration is expressed by two (not ideal) isosbestic points at ca. 490 nm and ca. 640 nm.

PM3 calculations and X-ray molecular structure: The calculated conformations of minimum energy for $\mathbf{2_{RED}}$ to $\mathbf{2_{OX}}^{+4}$ are given in Figure 12. In analogy to system **1** structures $\mathbf{2_{RED}}$, $\mathbf{2_{SEM}}^{\bullet+}$, and $\mathbf{2_{SEM}}^{\bullet+3}$ are closely related (Table 3). The bond lengths d_1-d_3 between the central four carbon atoms in $\mathbf{2_{RED}}$ show the typical distances of a 1,3-butadiene moiety (135, 145, 135 pm), which is smoothened out in $\mathbf{2_{SEM}}^{\bullet+}$ and $\mathbf{2_{SEM}}^{\bullet+3}$ (140 pm), but still keeping a planar conformation. In contrast to system **1**, however, two of the four 4-dimethylaminophenyl groups are found to be strongly twisted out of plane (64–90°) in $\mathbf{2_{RED}}$, $\mathbf{2_{SEM}}^{\bullet+}$, and $\mathbf{2_{SEM}}^{\bullet+3}$ whereas the two others are nearly in plane. Again the oxidation levels $\mathbf{2_{OX}}^{+2}$ and $\mathbf{2_{OX}}^{+4}$ look similar in shape: The two central carbon atoms now form a double bond ($d_2 = 134$ pm) and both ends show moieties of Michlers hydrol blue in a nearly perpendicular position ($\alpha_1 = \alpha_2$ are 70 and 37°, respectively) with much less twisted aromatic groups (4–44°).

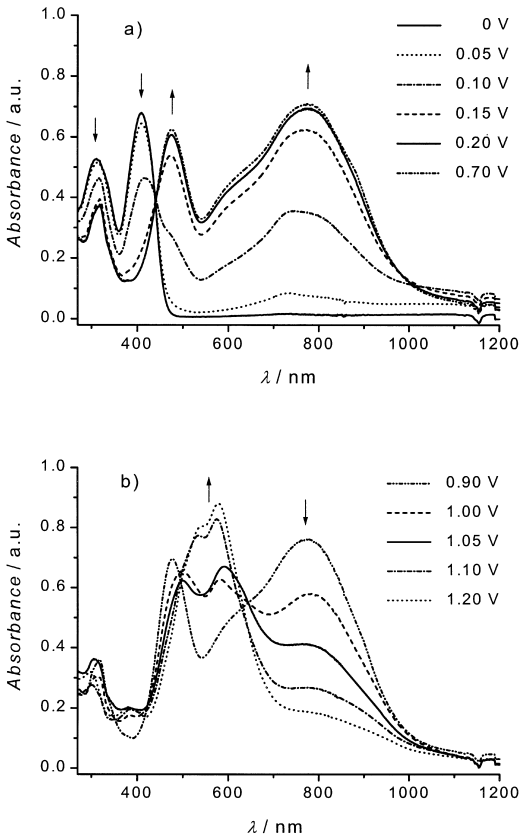

Figure 11. Spectroelectrogram of **2** on stepwise oxidation (CH_3CN, 0.1 M n-$Bu_4N^+PF_6^-$, potentials are given versus Ag/AgCl): a) $\mathbf{2_{RED}} \rightarrow \mathbf{2_{OX}}^{+2}$; b) $\mathbf{2_{OX}}^{+2} \rightarrow \mathbf{2_{OX}}^{+4}$.

X-ray single crystal structure of $\mathbf{2_{RED}}$ (Figure 13) shows excellent coincidence of d_1-d_3 bond lengths (135, 144, 135 pm) and central torsion angles (α_1, α_2, β) with calculated

Table 3. Parameters of PM3-optimized structures for compounds **2** at different oxidation levels and selected data for $\mathbf{2_{RED}}$ from single crystal X-ray determination.[a]

	$\mathbf{2_{RED}}$	$\mathbf{2_{RED}}$ (X-ray)	$\mathbf{2_{SEM}}^{\bullet+}$	$\mathbf{2_{OX}}^{2+}$	$\mathbf{2_{SEM}}^{\bullet 3+}$	$\mathbf{2_{OX}}^{4+}$(A)	$\mathbf{2_{OX}}^{4+}$(C)	$\mathbf{2_{OX}}^{4+}$(B)
Total energy [hartree]	−204.32878		−204.08746	−203.75450	−203.38349	−202.77171	−202.79558	−202.79855
Heat of formation [kcal mol^{-1}]	115.18		266.61	475.55	708.37	1092.27	1077.29	1075.43
HOMO [eV]	−7.73		−12.43		−16.10	−18.05	−18.72	
SOMO [eV]		−9.77 (α)[b]		−13.58 (α)				
		−10.19 (β)[b]		−13.69 (β)				
LUMO [eV]	−0.54		−4.29 (α)	−7.09	−8.99 (α)	−14.31	−12.06	−11.66
		−5.62 (β)		−9.64 (β)				
Dipole moment [Debye]	0.22		18.48	1.12	20.54	1.09	6.20	3.79
d_1 (C2−C1) [pm]	135.0	134.7(7)	140.5	147.8	139.9	146.8	146.0	150.7
d_2 (C1−C1a) [pm]	144.5	144.1(9)	140.0	133.7	140.8	134.4	134.2	157.6
d_3 (C1a−C2a) [pm]	135.0	134.7(7)	139.7	147.7	140.4	146.8	146.0	150.7
α_1 (C3-C2-C1-C1a) [°]	0.1	4.8	1.1	70.3	2.2	37.2	14.0	0.2
β (C2-C1-C1a-C2a) [°]	177.8	180.0	178.6	174.1	178.2	179.6	2.6	119.6
α_2 (C1-C1a-C2a-C3a) [°]	0.2	4.8	0.6	70.3	0.9	37.2	14.0	0.2
γ_A (C8-C3-C2-C1) [°]	84.5	65.7	74.1	13.1	63.5	44.4	74.0	110.3
γ_B (C17a-C12a-C2a-C1a) [°]	3.0	26.0	1.7	12.9	0.8	4.6	6.9	3.0
γ_C (C8a-C3a-C2a-C1a) [°]	89.9	65.7	76.5	21.8	86.1	44.4	74.0	110.3
γ_D (C17-C12-C2-C1) [°]	5.2	26.0	0.7	21.6	7.7	4.6	6.9	3.0

[a] Attribution of bond distances d_1-d_3 and torsion angles α_1, α_2, β, and γ_A-γ_D see in Figures 7 and 13. Signs of rotations for torsion angles are omitted; [b] orbital energies for α and β electrons.

0947-6539/00/0614-2624 $ 17.50+.50/0 *Chem. Eur. J.* **2000**, *6*, No. 14

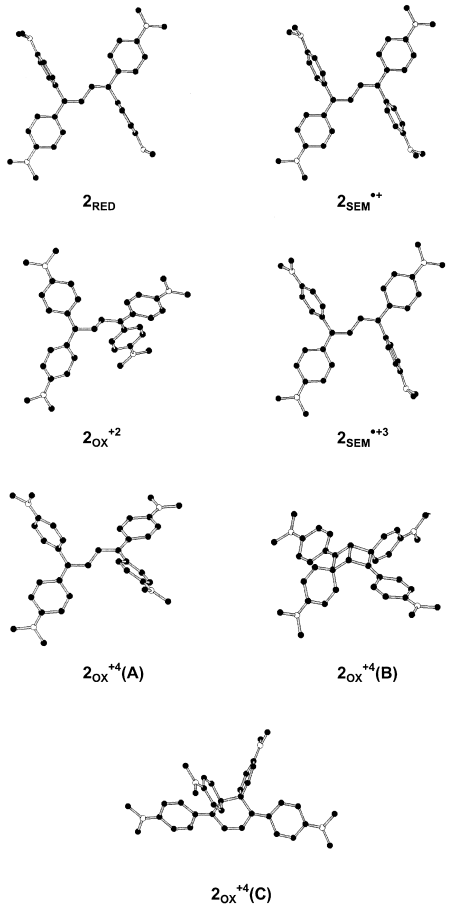

Figure 12. PM3-optimized geometries of compound **2** at various oxidation states (hydrogen atoms are omitted; closed circles are carbon atoms, open circles are nitrogen atoms).

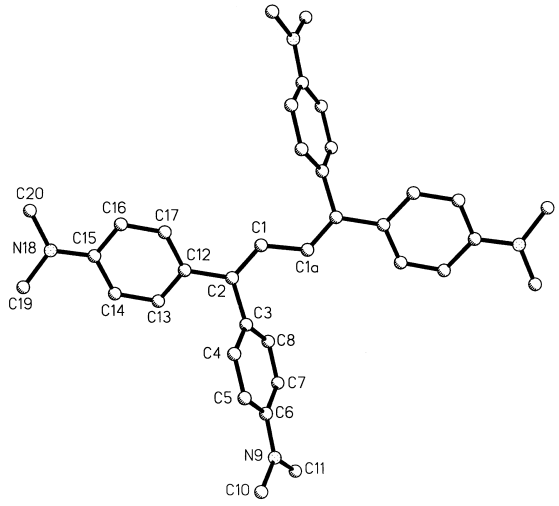

Figure 13. Single crystal X-ray molecular structure of $\mathbf{2_{RED}}$.

values. Similarly to compound $\mathbf{1_{RED}}$, calculated values of rotations of phenyls ($\gamma_A \approx \gamma_C \approx 85-90^\circ$, $\gamma_B \approx \gamma_D \approx 3-5^\circ$) somewhat differ in their absolute values from the X-ray data ($\gamma_A = \gamma_C = 66^\circ$, $\gamma_B = \gamma_D = 26$) probably due to crystal packing of the molecule. However, in general, X-ray structural and theoretical results are in good agreement: Two phenyls (**B** and **D**; Figure 7) tend to be in plane and the two others (**A** and **C**) are substantially distorted.

Similar to system **1** the weight of the presented PM3 optimized conformations of system **2** should not be overestimated, since their energy minima are rather shallow with other conformations of only slightly higher energy (1–2 kcal mol^{-1} or even less) easily available; this demonstrates a high flexibility of these molecules. For $\mathbf{2_{OX}^{+4}}$ a closer inspection of charge localization/bond alteration reveals that it may form a new single bond yielding structures with a central six-membered ring or with two annelated four-membered rings (Figure 12). This way bicyclic structure $\mathbf{2_{OX}^{+4}(B)}$ is derived from (*E*)-$\mathbf{2_{OX}^{+4}}$ and monocyclic structure $\mathbf{2_{OX}^{+4}(C)}$ from (*Z*)-$\mathbf{2_{OX}^{4+}}$ (Figure 12). Indeed, according to calculations, both cyclized isomers are more stable by 16.84 and 14.98 kcal mol^{-1}, respectively (Table 3). $\mathbf{2_{OX}^{+4}(C)}$ (monocyclic) could well be responsible for the absorption band at 590 nm on Figure 11b.

Higher vinylogues of $\mathbf{2_{OX}^{+2}}$ have just been reported without referring to their redox properties.[14]

System 3

This system corresponds to **2** in which the carbon atoms of the two central methine groups are replaced by two nitrogen atoms. Therefore in system **3** somewhat higher configurational flexibility and different electron affinities are to be expected.

Synthesis: This bis-aza derivative of **2**, 1,1,4,4-tetrakis(4-dimethylaminophenyl)-2,3-diaza-1,3-butadiene ($\mathbf{3_{RED}}$), the azine of Michlers ketone, was prepared as described,[15] although the starting material, the hydrazone of Michlers ketone[15] is more reliably obtained from thio-Michlers ketone and hydrazine.

Electrochemistry and ESR: Again, the cyclic voltammogram of $\mathbf{3_{RED}}$ shows two reversible redox waves, similar to system **2** (Figure 14). However, $E_{1/2}{}^1 = 166$ mV is more positive and with $E_{1/2}{}^2 = 673$ mV, $\Delta E_{1/2}{}^{1-2} = 507$ mV being dramatically reduced. This effect of the two nitrogen atoms in the central chain is well documented in the violene series.[4c] In both steps two electrons must be transferred. Similar to systems **1** and **2**

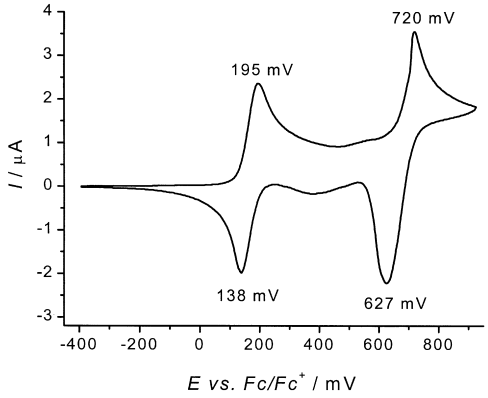

Figure 14. Cyclic voltammogram of $\mathbf{3_{RED}}$ in CH_2Cl_2/*n*-$Bu_4N^+PF_6^-$ (0.1M) versus Fc/Fc^+. Scan rate 100 mV s^{-1}.

only traces of $\mathbf{3}_{\mathbf{SEM}}^{\bullet+}$ can be detected by its ESR signal (Figure 15). As for $\mathbf{1}_{\mathbf{SEM}}^{\bullet+}$, and $\mathbf{2}_{\mathbf{SEM}}^{\bullet+}$ also for $\mathbf{3}_{\mathbf{SEM}}^{\bullet+}$ the spin and the charge are delocalized over the entire π-system on the hyperfine time scale; this indicates two-fold symmetry. Temperature variation does not indicate any dynamic process which may disturb this symmetry.

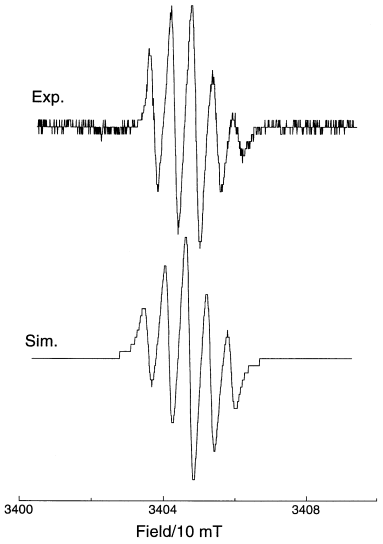

Figure 15. ESR spectrum of $\mathbf{3}_{\mathbf{SEM}}^{\bullet+}$ and its simulation.

For $\mathbf{3}_{\mathbf{SEM}}^{\bullet+}$, however, the theoretical and the experimental values deviate substantially. The calculations (cf. Computational section) predict a dominating amount of the spin population in the C=N-N=C moiety with a ^{14}N hfc of 1.5 mT. In contrast to its iso-π-electronic isomer **2**, the calculations provide somewhat smaller twist of the 4-dimethylaminophenyl substituents with only a negligible spin transfer into the latter group (Figure 16). Whereas the ESR parameters are in very good agreement with a virtually non-detectable spin in the aryl groups, a discrepancy exists for the ^{14}N hfc: The experimental value of 0.058 mT is far off its calculated counterpart (1.5 mT). Unfortunately, the spin population at the carbon atoms can not be detected because the signal intensity is too low to establish the determination of ^{13}C isotopes. Comparison of the electronic spectra detected simultaneously with the ESR signal indicates that no more starting material is present: The absorption points to a chemical oxidation of $\mathbf{3}_{\mathbf{RED}}$ to mono-tetra cations. None of the paramagnetic redox stages, however, is in accord with the observed small ^{14}N hfc. Therefore the description of $\mathbf{3}^{\bullet+}$ remains equivocal.

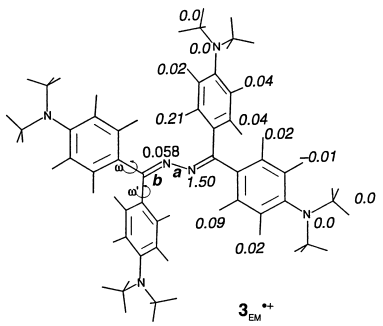

Figure 16. Experimental (displayed in the upper right moieties) and calculated (UB3LYP/6–31G*//UHF/3–21G*, in italics; displayed in the lower right moieties) hfcs determined for $\mathbf{3}_{\mathbf{SEM}}^{\bullet+}$: $a = 133.3$ pm, $b = 129.0$ pm, $\omega = 17.2°$, $\omega' = 47.5°$.

Starting oxidation of $\mathbf{3}_{\mathbf{RED}}$ the spectroelectrogram in Figure 17a clearly shows equilibration of two species by a well defined isosbestic point at 410 nm. The yellow $\mathbf{3}_{\mathbf{RED}}$ (↓340 nm, ↓385 nm) is stepwise replaced by violet $\mathbf{3}_{\mathbf{OX}}^{+2}$ [↑460 nm, ↑510 nm (shoulder)] and finally a new low absorption band at 610 nm appears, which obviously represents a new species (probably $\mathbf{3}_{\mathbf{OX}}^{+4}$) as can be judged from Figure 17b. Here on further oxidation, $\mathbf{3}_{\mathbf{OX}}^{+2}$ is consumed at the cost of probably $\mathbf{3}_{\mathbf{OX}}^{+4}$ [(↑560 nm (shoulder), ↑600 nm]. Besides another very broad absorption band is produced around 800–900 nm with broad extension into IR region (Figure 17).

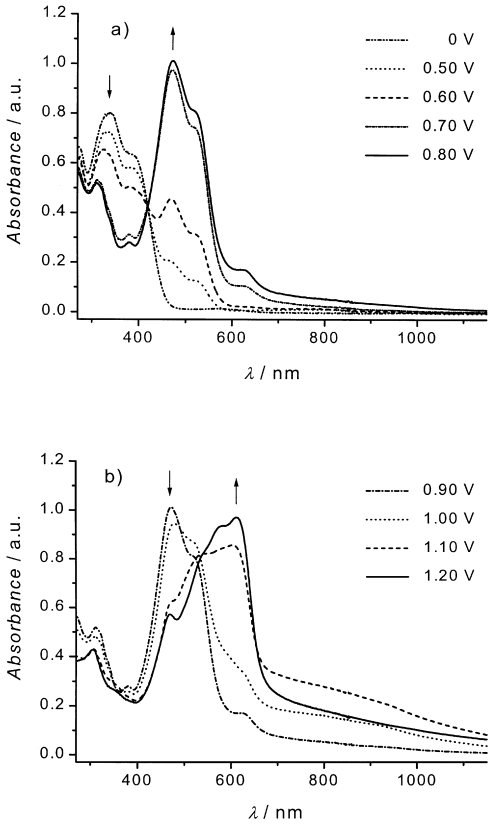

Figure 17. Spectroelectrogram of **3** on stepwise oxidation (CH_3CN, 0.1 M n-$Bu_4N^+PF_6^-$, potentials are given versus Ag/AgCl): a) $\mathbf{3}_{\mathbf{RED}} \rightarrow \mathbf{3}_{\mathbf{OX}}^{+2}$; b) $\mathbf{3}_{\mathbf{OX}}^{+2} \rightarrow \mathbf{3}_{\mathbf{OX}}^{+4}$.

The two nitrogen atoms in the backbone of **3** modify the UV/Vis absorption considerably compared with system **2**: The longest wavelength absorption in **2** is shown by $\mathbf{2}_{\mathbf{OX}}^{+2}$ (760 nm) but not for $\mathbf{3}_{\mathbf{OX}}^{+2}$ (510 nm). Here a higher oxidation level of **3** (probably OX^{+4}) presents the most bathochromic shift (ca. 600 nm).

PM3 calculations and X-ray molecular structure: As to be expected the geometries of $\mathbf{3}_{\mathbf{RED}}$ to $\mathbf{3}_{\mathbf{OX}}^{+4}$ (Table 4, Figure 18) resemble those of system **2**. Again the four central atoms stay

  0947-6539/00/0614-2626 $ 17.50+.50/0 *Chem. Eur. J.* **2000**, *6*, No. 14

Table 4. Parameters of PM3-optimized structures for compounds **3** at different oxidation levels and selected data for $\mathbf{3}_{\mathbf{RED}}$ from single crystal X-ray determination.[a]

	$\mathbf{3}_{\mathbf{RED}}$	$\mathbf{3}_{\mathbf{RED}}$ (X-ray)	$\mathbf{3}_{\mathbf{SEM}}{}^{\bullet+}$	$\mathbf{3}_{\mathbf{OX}}{}^{2+}$	$\mathbf{3}_{\mathbf{SEM}}{}^{\bullet 3+}$	$\mathbf{3}_{\mathbf{OX}}{}^{4+}$(A)	$\mathbf{3}_{\mathbf{OX}}{}^{4+}$ (C)	$\mathbf{3}_{\mathbf{OX}}{}^{4+}$(B)
Total energy [hartree]	−206.38239		−206.12927	−205.79887	−205.42316	−204.81595	−204.83303	−204.82135
Heat of formation [kcal mol^{-1}]	142.88		301.72	509.05	744.81	1125.85	1115.14	1122.46
HOMO [eV]	−8.15			−12.56		−16.23	−18.44	−18.50
SOMO [eV]			−9.83(α)[b]		−13.60(α)			
			−10.18(β)[b]		−13.70(β)			
LUMO [eV]	−0.48		−4.29(α)	−7.27	−9.15(α)	−14.38	−12.10	−11.84
		−5.76(β)		−9.63(β)				
Dipole moment [Debye]	0.96		19.84	0.12	20.07	0.81	8.33	5.33
d_1 (C2–N1) [pm]	130.7	129.9(3)	136.2	144.3	134.5	145.9	145.2	145.9
d_2 (N1–N1a) [pm]	138.5	139.7(4)	131.8	122.2	133.2	122.6	121.7	152.6
d_3 (N1a–C2a) [pm]	130.7	129.9(3)	135.1	144.2	135.3	145.9	145.2	145.9
α_1 (C3-C2-N1-N1a) [°]	0.0	3.6	0.5	89.3	0.7	46.4	13.4	0.5
β (C2-N1-N1a-C2a) [°]	179.9	180.0	180.0	179.9	175.9	178.3	1.6	123.7
α_2 (N1-N1a-C2a-C3a) [°]	0.0	3.6	0.5	90.0	1.2	45.2	13.4	0.5
γ_A (C8-C3-C2-N1) [°]	84.8	48.3	82.8	37.4	88.0	51.2	78.6	108.2
γ_B (C17a-C12a-C2a-N1a) [°]	31.1	18.1	1.0	17.5	11.1	6.9	177.3	6.3
γ_C (C8a-C3a-C2a-N1a) [°]	85.1	48.3	88.4	37.1	88.1	51.4	78.6	108.2
γ_D (C17-C12-C2-N1) [°]	31.2	18.1	0.2	17.4	3.0	7.0	2.6	6.3

[a] Attribution of bond distances d_1–d_3 and torsion angles α_1, α_2, β, and γ_A-γ_D see in Figures 7 and 19. Signs of rotations for torsion angles are omitted; [b] orbital energies for α and β electrons.

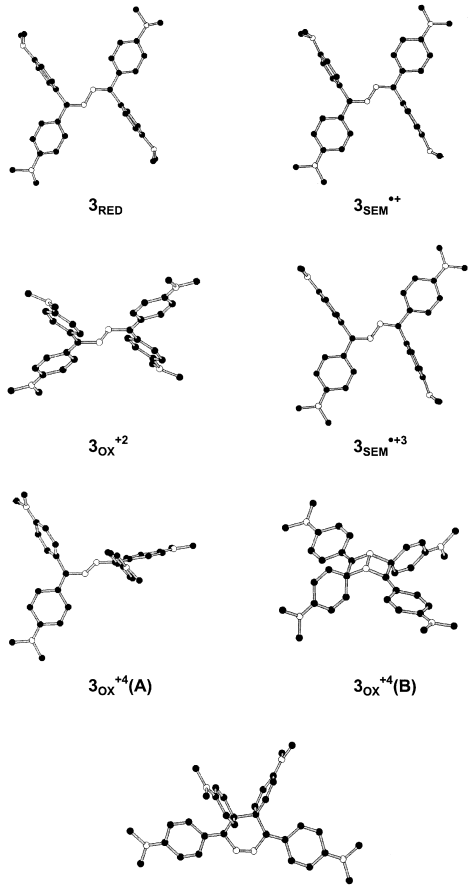

Figure 18. PM3-optimized geometries of compound **3** at various oxidation states (hydrogen atoms are omitted; closed circles are carbon atoms, open circles are nitrogen atoms).

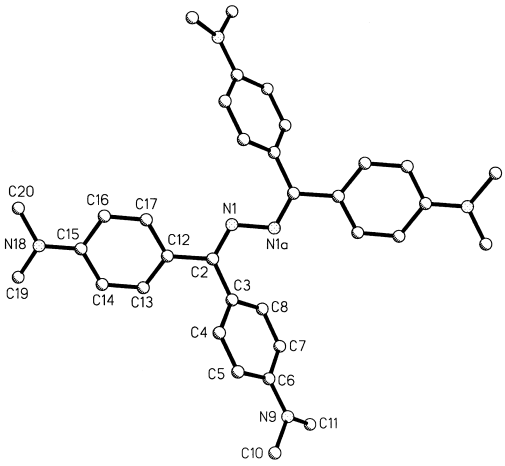

Figure 19. Single crystal X-ray molecular structure of $\mathbf{3}_{\mathbf{RED}}$.

planar in $\mathbf{3}_{\mathbf{RED}}$, $\mathbf{3}_{\mathbf{SEM}}{}^{\bullet+}$, and $\mathbf{3}_{\mathbf{SEM}}{}^{\bullet+3}$ with two C=N double bonds ($d_1 = d_3 = 131$ pm) and one N–N single bond ($d_2 = 139$ nm) in $\mathbf{3}_{\mathbf{RED}}$ and equalized distances in $\mathbf{3}_{\mathbf{SEM}}{}^{\bullet+}$ and $\mathbf{3}_{\mathbf{SEM}}{}^{\bullet+3}$. Experimental (X-ray single crystal structure, Figure 19 and Table 4) bond lengths ($d_1 = d_3 = 130$ pm, $d_2 = 140$ pm) as well as torsion angles at the four central atoms of $\mathbf{3}_{\mathbf{RED}}$ (α_1, α_2, and β) correspond well to PM3 predicted values.

Compared with $\mathbf{2}_{\mathbf{RED}}$, again two of the four aromatic moieties in these species are calculated to be strongly twisted out of plane: ($\gamma_A = \gamma_C = 85°$, $\gamma_B = \gamma_D = 31°$), whereas the X-ray data (Figure 19) present a much more flattened molecule ($\gamma_A = \gamma_C = 48°$, $\gamma_B = \gamma_D = 18°$). Similarly to $\mathbf{1}_{\mathbf{RED}}$ and $\mathbf{2}_{\mathbf{RED}}$, experimental twisting in the crystal is lower than PM3 calculated values. By contrast to $\mathbf{3}_{\mathbf{RED}}$, $\mathbf{3}_{\mathbf{SEM}}{}^{\bullet+}$, and $\mathbf{3}_{\mathbf{SEM}}{}^{\bullet+3}$, in $\mathbf{3}_{\mathbf{OX}}{}^{2+}$ and to somewhat lesser extend in $\mathbf{3}_{\mathbf{OX}}{}^{+4}$ the two Michlers hydrol end groups occupy substantial out-off-plane positions to the central chain (α_1 and α_2 are $\approx 90°$ and $\approx 45°$, respectively) and the differences between the torsion angles γ_A, γ_B, and γ_B, γ_C are much less; this allows better delocalization of the π-electrons. Similar to $\mathbf{2}_{\mathbf{OX}}{}^{+4}$ two structures of lower energy are found for tetracation $\mathbf{3}_{\mathbf{OX}}{}^{4+}$, that is bicyclic $\mathbf{3}_{\mathbf{OX}}{}^{+4}$**(B)** ($-3.39$ kcal mol^{-1}) and monocyclic $\mathbf{3}_{\mathbf{OX}}{}^{+4}$**(C)** ($-10.71$ kcal mol^{-1}) (Figure 18, Table 4). Therefore the latter cyclic structure seems to be the preferred one for $\mathbf{3}_{\mathbf{OX}}{}^{+4}$.

System 4

In systems **1–3** both ends become cyanines of the Michlers hydrol type on oxidation to the dications. We wondered which electrochromic properties would arise if only one end group is turned into such a low energy cyanine. System **4** was chosen as a suitable test compound.

Synthesis: On treating 2-hydrazono-3-methyl-2,3-dihydrobenzothiazole (**7**) with thio-Michlers ketone (**8**) the new redox system $\mathbf{4_{RED}}$ is formed (Scheme 4).

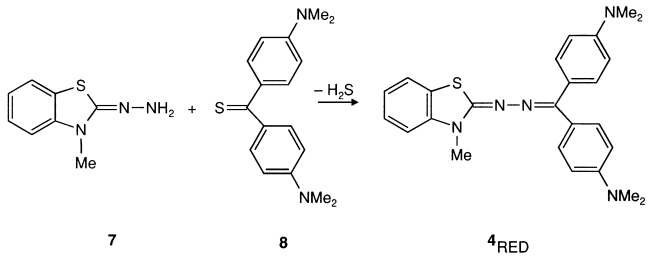

Scheme 4. Synthesis of $\mathbf{4_{RED}}$.

Electrochemistry: Cyclic voltammetry of $\mathbf{4_{RED}}$ reveals two completely reversible redox waves which correspond to two single electron transfers as judged from intensity as compared with an equivalent of ferrocene (not shown in Figure 20a). A third much more positive oxidation peak at about 800 mV is found nearly irreversible (electrochemically) at the scan rate of 25 or 100 mV s^{-1} (Figure 20b). The whole redox cycle, however, represents chemically reversible reactions since the cyclic voltammogram remains unchanged on repeated scans. Moreover, the third oxidation potential approaches electrochemical reversibility with increasing scan rate up to 1000 mV s^{-1} (Figure 20b). The *reversible* redox process therefore can be described as shown in Scheme 5.

System **4** obviously behaves as a typical violene system[4] with $K_{SEM} = 4.6 \times 10^3$ L mol^{-1} probably due to its asymmetrical structure in which the stabilization of $\mathbf{4_{OX}}^{+2}$ by the benzothiazolium moiety is not sufficient. Nevertheless, as demonstrated by the spectroelectrogram (Figure 21a–c) the cyanine character of $\mathbf{4_{OX}}$ with its long wavelength absorption is well developed.

Starting from $\mathbf{4_{RED}}$ with $\lambda_{max} = 330$, 380 nm on stepwise oxidation (Figure 21a) $\mathbf{4_{RED}}$ equilibrates (isosbestic points at 280 and 405 nm) with a second species ($\lambda_{max} = 555$ and 440 nm) which must be $\mathbf{4_{SEM}}^{\bullet+}$. On further oxidation (Figure 21b) the absorption at 330 nm is slightly increased and a strong absorption band at $\approx$460 nm appears whereas the absorption at $\approx$555 nm stays nearly constant and a low but very broad absorption beyond 700 nm also arises with a peak around 1150 nm. Finally (Figure 21c), new isosbestic points at $\approx$405 and 490 nm are created when the maxima at 340 nm and 530 nm are growing on cost of λ_{max} $\approx$470 nm. The latter must be caused by $\mathbf{4_{OX}}^{+2}$ together with the band around 700 nm (probably intramolecular charge transfer). This interpretation implies that the longest wavelength absorption in Figures 21a and 21c belong to $\mathbf{4_{SEM}}^{\bullet+}$ and $\mathbf{4_{OX}}^{+2}$, respectively, being similar by accident. The species from the higher oxidation potential [E_p ca. 750 mV (Figure 20b)] cannot be safely discerned in the spectroelectromgram of Figure 22.

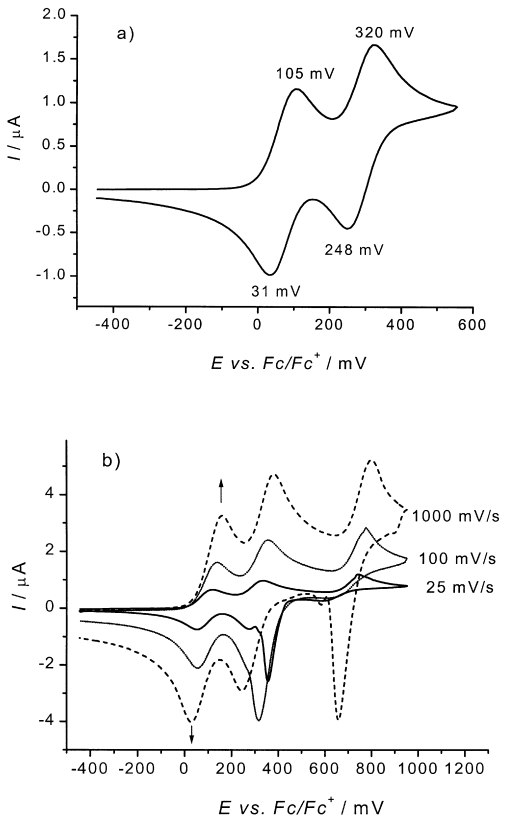

Figure 20. Cyclic voltammogram of $\mathbf{4_{RED}}$ in CH_2Cl_2/*n*-$Bu_4N^+PF_6^-$ (0.1M) versus Fc/Fc$^+$: a) $\mathbf{4_{RED}} \rightarrow \mathbf{4_{SEM}}^{\bullet+} \rightarrow \mathbf{4_{OX}}^{+2}$, scan rate 100 mV s^{-1}; b) CV at scan rates 25, 100, and 1000 mV s^{-1}.

PM3 calculations: The results of the PM3 optimizations of the structures **4** are summarized in Table 5 and corresponding conformations are shown in Figure 22. In the asymmetrical system **4** the geometries of the different oxidation levels show some peculiarities: In $\mathbf{4_{RED}}$, $\mathbf{4_{SEM}}^{\bullet+}$, and $\mathbf{4_{SEM}}^{\bullet+3}$ one aryl group occupies a position perpendicular ($\gamma_B \approx 81-89°$) to the rest of the molecule with a coplanar C-N-N-C backbone. In $\mathbf{4_{OX}}^{+2}$ and $\mathbf{4_{OX}}^{+4}$, however, the two aromatic groups form the typical moiety of Michlers hydrol blue twisted by 97° and 84°, respectively, from the central N-N-C unit. A cyclic structure $\mathbf{4_{OX}}^{+4}$**(C)** can be formulated for this oxidation level (Figure 22)

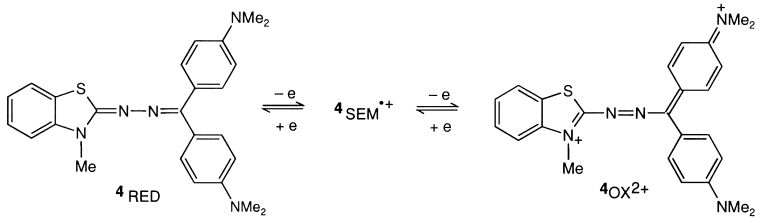

Scheme 5. Redox system **5**.

0947-6539/00/0614-2628 $ 17.50+.50/0 *Chem. Eur. J.* **2000**, *6*, No. 14

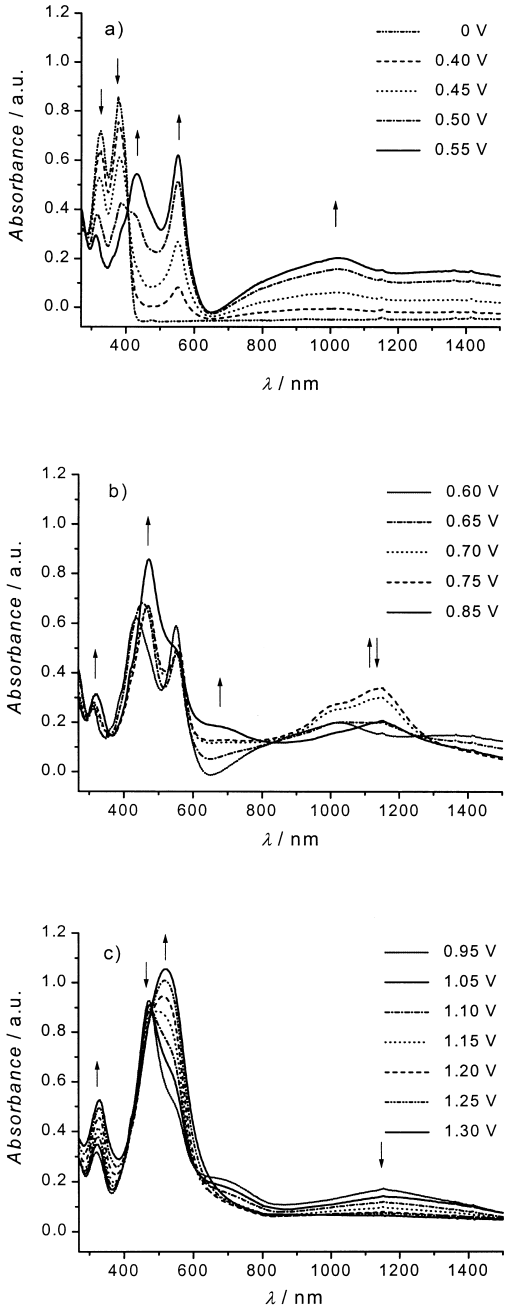

Figure 21. Spectroelectrogram of **4** on stepwise oxidation (CH_3CN, 0.1 *n*-$Bu_4N^+PF_6^-$, potentials are given versus Ag/AgCl): a) $\mathbf{4_{RED}} \rightarrow \mathbf{4_{SEM}}^{\bullet+}$; b) $\mathbf{4_{SEM}}^{\bullet+} \rightarrow \mathbf{4_{OX}}^{+2}$; c) $\mathbf{4_{OX}}^{+2} \rightarrow \mathbf{4_{SEM}}^{\bullet+3}$ ($\mathbf{4_{OX}}^{+4}$).

which, however, in contrast to systems **1**–**3**, was found to be of higher energy by 22.3 kcal mol^{-1} than acyclic structure $\mathbf{4_{OX}}^{+4}$**(A)**, probably due to the one positive charge which has to be ascribed to one of the two azo nitrogen atoms making the four-membered ring to be very strained.

Conclusion

The general structure **A** for violene/cyanine hybrids is well expressed by compounds in which the end groups X and Y are represented by 4-dialkylaminophenyl moieties. This structure enables systems $\mathbf{1_{RED}}$, $\mathbf{2_{RED}}$, and $\mathbf{3_{RED}}$ to produce two highly colored cyanine systems on forming OX^{+2}. Gain of energy in formation of these cyanine systems is so strong that on oxidation $\mathbf{1}$–$\mathbf{3_{RED}}$ radical ions SEM can be detected only in traces. Reliable spin density distributions could be assigned for $\mathbf{1_{SEM}}^{\bullet+}$ and $\mathbf{2_{SEM}}^{\bullet+}$ in agreement with ab initio calculations. By contrast, system **4** which contains one end group typical for violenes[4] and the other one for cyanines behaves as a definite two step redox system of the violene type ($K_{SEM} = 4.6 \times 10^3$ L mol^{-1}), however, also with the longest wavelength absorption of the closed shell oxidation level OX^{+2}. Higher oxidation levels are observed in all cases but they display lower reversibility.

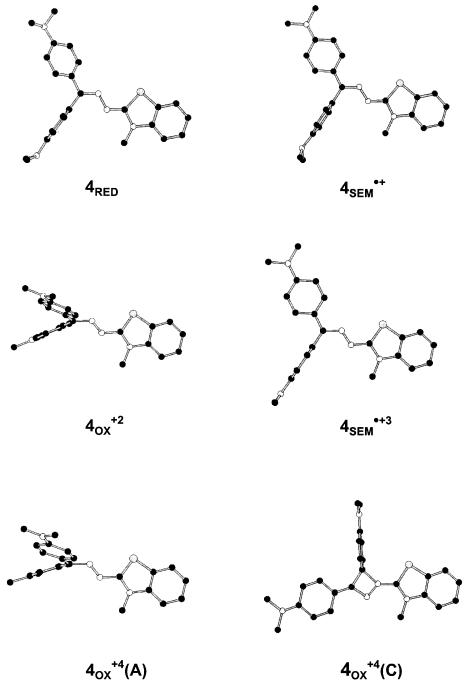

Figure 22. PM3-optimized geometries of compound **4** at various oxidation states (hydrogen atoms are omitted; closed circles are carbon atoms, open circles are nitrogen atoms, grey circles are sulfur atoms).

The anticipated strong twist around the central bonds on going from RED to OX^{+2} is supported by PM3 calculations which substantiate the cyanine type moieties in $\mathbf{1}$–$\mathbf{4_{OX}}^{+2}$. Similar structures are found for $\mathbf{1}$–$\mathbf{4_{OX}}^{+4}$; however in the case of $\mathbf{1}$–$\mathbf{3_{OX}}^{+4}$ these acyclic structures (A) are of much higher energies than isomeric cyclic ones (C or B) in which new single bonds have been formed. In contrast, for system **4**, PM3 calculations predict the acyclic structure $\mathbf{4_{OX}}^{+4}$**(A)** to be more stable than the cyclic structure $\mathbf{4_{OX}}^{+4}$**(C)**. Due to their reversibility, formation of closed shell systems within the redox cycle and the strong differences in absorption systems **1**–**3** (and **4**) may be valuable candidates for electrochromic systems.

Experimental Section

General: Melting points were determined on a hot-stage microscope (Fa. Reichert) and are corrected. IR: Perkin–Elmer 1420 spectrophotometer. ^{1}H and ^{13}C NMR: Bruker AC 200 and AC 250 spectrometers; standardized by solvent signals unless indicated. MS: Varian MT CH7 and Finnigan MAT 8200 spectrometers.

Table 5. Parameters of PM3-optimized structures for compounds **4** at different oxidation levels.[a]

	$\mathbf{4}_{RED}$	$\mathbf{4}_{SEM}^{\bullet+}$	$\mathbf{4}_{OX}^{2+}$	$\mathbf{4}_{SEM}^{\bullet 3+}$	$\mathbf{4}_{OX}^{4+}$(A)	$\mathbf{4}_{OX}^{4+}$(C)
Total energy [hartree]	−160.70687	−160.45638	−160.10767	−159.70829	−159.07619	−159.04066
Heat of formation [kcal mol^{-1}]	134.36	291.55	510.38	760.99	1157.65	1179.95
HOMO [eV]	−8.04		−12.77		−18.59	−19.63
SOMO [eV]	−10.55 (α)[b]		−16.65 (α)			
	−10.62 (β)[b]		−16.55 (β)			
LUMO [eV]	−0.46	−4.50 (α)	−7.99	−9.94 (α)	−15.22	−14.42
	−5.46 (β)		−10.17 (β)			
Dipole moment [Debye]	1.96	4.98	3.89	13.63	20.80	13.17
d_1 [pm]	130.7	136.9	144.7	138.4	146.4	141.8
d_2 [pm]	137.7	129.2	122.4	127.5	122.8	128.6
d_3 [pm]	130.9	137.3	144.8	140.8	1437	142.5
α_1 [°]	0.0	1.0	97.4	4.4	83.5	0.0
β [°]	179.9	179.7	179.2	177.9	179.6	180.0
α_2 [°]	0.9	0.6	16.8	4.8	6.3	179.1
γ_A [°]	37.7	1.3	25.8	0.5	16.4	0.0
γ_B [°]	86.5	81.1	26.2	89.3	16.3	110.7
γ_C [°]	23.1	0.3	2.8	1.0	1.4	0.1

[a] Attribution of bond distances d_1-d_3 and torsion angles α_1, α_2, β, and γ_A-γ_C see in Figure 7. Signs of rotations for torsion angles are omitted; [b] orbital energies for α and β electrons.

Tetrakis(4-dimethylaminophenyl)ethene ($\mathbf{1}_{RED}$): The crude product (≈21 g) obtained from Michlers ketone (14.2 g, 52 mmol)[5] was dissolved in dichloromethane/petrol ether 1:2, filtered through a pad of Alox BIII and the solvent removed. Recrystallization from toluene/ethanol 2:1 yielded $\mathbf{1}_{RED}$ (10.1 g, 75%) with m.p.: 292 °C (ref.[5]: m.p.: 275 °C); ^{1}H NMR (200.1 MHz, $C_6D_5CD_3$): $\delta = 2.80$ (s, CH_3, 24H), 6.51 (d, *o*-Ph, 8H), 6.95 (d, *m*-Ph, 8H); ^{13}C NMR (50.6 MHz, $CDCl_3$): $\delta = 40.5$ (CH_3), 113.0 (*o*-C), 132.4 (C-1, C-2, and *p*-C), 134.0 (*m*-C), 148.2 (*i*-C); $C_{34}H_{40}N_4$ (504.96): calcd C 80.88, H 7.99, N 11.13; found C 80.97, H 7.86, N 11.04%.

Tetrakis(4-dimethylaminophenyl)ethenium bis(tetrafluoroborate) ($\mathbf{1}_{OX}^{+2}\cdot 2BF_4^-$): In adaption of ref.[6] to **1** (250 mg, 0.50 mmol) in acetic acid (3 mL) was added dropwise lead(IV) acetate (250 mg, 0.56 mmol) in acetic acid (5 mL). After addition of water (22 mL) to the dark blue solution, containing sodium tetrafluoroborate (220 mg, 2.0 mmol) black crystals were deposited (320 mg, 94%). The compound was purified from acetic acid yielding $\mathbf{1}_{OX}^{+2}\cdot 2BF_4^-$ (217 mg, 64%), m.p.: 230 °C (dec.); IR (KBr): = 1575, 1475, 1355, 1160, 1095 cm^{-1}; ^{1}H NMR (200 MHz, CD_3NO_2): δ (broad signals) = 3.40 (CH_3, 24H), 7.05, 7.64 (Ph, 16H); $C_{34}H_{40}N_4B_2F_8$ (678.3): calcd C 60.20, H 5.94, N 8.25; found C 59.73, H 6.07, N 7.95%.

1,1,4,4-Tetrakis(4-dimethylaminophenyl)-1,3-butadiene ($\mathbf{2}_{RED}$): Lead(IV) tetraacetate (2.05 g, 4.06 mmol) in chloroform (15 mL) was slowly added to 1,1-bis(4-dimethylaminophenyl)ethene **6** (1.33 g, 5.00 mmol) in chloroform (5 mL). After 30 min the dark green solution was treated with potassium carbonate (5 g) and filtered through a pad of Alox BIII. The solvent was removed and the residue was chromatographed on Alox BIII (DCM/PE, 1:1). Crude $\mathbf{2}_{RED}$ was isolated from the second fraction as an orange oil (1.0 g) which was crystallized from acetone/ethanol yielding light yellow crystals (900 mg, 70%). M.p.: 270 °C (ref.[13], m.p.: 282 °C); IR (KBr): $\tilde{\nu} = 1605$, 1520, 1350, 950, 820 cm^{-1}; ^{1}H NMR (200.1 MHz, $C_6D_5CD_3$): $\delta = 2.70$ (br s, CH_3), 2.77 (br s, CH_3), 6.6 (d, C=CH-), 6.8 (d, *o*-Ph), 7.6 (d, *m*-Ph); ^{13}C NMR (50.32 MHz): $\delta = 41.0$ (CH_3), 113.5/113.3 (*o*-C), 133.3 (*p*-C), 143.7 (*m*-C), 150.8 (*i*-C); $C_{36}H_{42}N_4$ (531.0): calcd 81.43, H 7.97, N 10.59; found C 81.34, H 8.23, N 10.10%.

4,4′-Bis(dimethylamino)benzophenone azine ($\mathbf{3}_{RED}$): a) The hydrazone of Michlers ketone was prepared in the literature by heating Michlers ketone with excess of hydrazine and calcium oxide.[15] Since we were not able to isolate a pure product we heated thio-Michlers ketone **8** (6.95 g, 24.4 mmol) and hydrazine hydrate (100%), (1.84 g, 36.0 mmol) in dry ethanol under reflux (30 min). The solution was concentrated to 50 mL and cooled to 0 °C. Isolation of the yellow crystals yielded 4,4′-bis(dimethylamino)benzophenone hydrazone (5.59 g, 81%). M.p.: 143–145 °C (ref.[15]: m.p.: 149 °C); b) in adaptation of ref.[15], 4,4′-bis(dimethylamino)benzophenone hydrazone (5.00 g, 17.7 mmol) was pulverized and heated to 150–160 °C for 3 h. The isolated brownish solid (4.40 g, 93%) was recrystallized from toluene yielding $\mathbf{3}_{RED}$ (3.80 g, 81%) as brown red crystals, m.p.: 256–258 °C (ref.[15]: m.p.: 253 °C); ^{1}H NMR (250 MHz, $CDCl_3$, TMS): $\delta = 2.98$ (s, CH_3, 24H), 6.66 (t, *m*-Ph, 8H), 7.38 (d, $J = 3.5$ Hz, *o*-Ph, 4H), 7.52 (d, $J = 3.5$ Hz, *o*-Ph, 4H); ^{13}C NMR (63 MHz, $CDCl_3$): $\delta = 40.3$ (q, 8 CH_3), 110.8 (d, 4 CH), 111.2 (d, 4 CH), 124.0 (s, 2 C), 128.1 (s, 2 C), 130.3 (d, 4 CH), 131.8 (d, 4 CH), 150.2 (s, 2 C), 150.8 (s, 2 C), 159.4 (s, 2 C, C=N-N=C); IR (KBr): $\tilde{\nu} = 2885$ (w), 2850 (w), 2795 (w), 1605 (s), 1566 (m), 1515 (s), 1445 (w), 1355 (s), 1323 (m), 1310 (w), 1225 (w), 1187 (s), 947 (m), 825 cm^{-1} (s); MS (70 eV): *m/z* (%): 533 (2) $[M]^+$, 532 (7), 531 (3), 413 (2), 412 (6), 386 (1), 267 (3), 266 (6), 251 (3), 250 (2), 237 (1), 223 (2), 206 (1), 193 (1); $C_{34}H_{40}N_6$ (537.7): calcd C 76.66, H 7.57, N 15.76; found C 76.44, H 7.69, N 15.77%.

4,4′-Bis(dimethylamino)benzophenone *N*-methylbenzothiazol-2(3H)-one azine ($\mathbf{4}_{RED}$): Thio-Michlers ketone **8** (2.83 g, 10.0 mmol) and 2-hydrazono-3-methyl-2,3-dihydrobenzothiazole (**7**, 1.79 g, 10.0 mmol) were heated to reflux in ethanol (100 mL) for 12 d. The crude product (3.85 g, 90%) was isolated from the cooled solution, m.p.: 185–190 °C. From ethyl acetate pale yellow crystals of $\mathbf{4}_{RED}$ (2.87 g, 67%) were obtained, m.p.: 190–192 °C; IR (KBr): $\tilde{\nu} = 3070$ (w), 2900 (w), 2800 (w), 1595 (s), 1578 (s), 1555 (m), 1440 (w), 1354 (m), 1325 (m) 1228 (m), 1198 (m), 1168 (m), 1157 (m), 1028 (m), 945 (m), 848 (m), 818 (s), 744 cm^{-1} (s); MS (70 eV): *m/z* (%): 430 (5) $[M]^+$, 429 (16), 253 (2), 252 (12), 237 (4), 200 (2), 126 (10), 125 (2), 188 (2); ^{1}H NMR (250 MHz, $CDCl_3$, TMS): $\delta = 2.96$ [d, $N(CH_3)_2$, 6H], 2.98 [d, $N(CH_3)_2$, 6H], 3.41 (s, benzothiazole N-CH_3, 3H), 6.64–6.73 (m, 4H), 6.84–6.98 (m, 2H), 7.14–7.20 (m, 1H), 7.33–7.36 (m, 1H), 7.45 (d, $J =$ 8.9 Hz, 2H), 7.63 (d, $J = 9.2$ Hz, 2H); ^{13}C NMR (63 MHz, $CDCl_3$, TMS): $\delta = 30.9$ (q, benzothiazole N-CH_3), 40.4 (q, 4 CH_3), 108.5 (d, CH), 110.7 (d, CH), 111.5 (d, CH), 120.9 (d, CH), 122.1 (d, CH), 123.9 (s, C), 125.3 (s, C), 125.7 (d, CH), 127.9 (s, C), 130.1 (d, CH), 132.0 (d, CH), 141.6 (s, C), 150.1 (s, C-NMe_2), 159.5 (s, Ar_2=C-N), 164.8 [s, C(2)-benzothiazole]; $C_{25}H_{27}N_5S$ (429.9): calcd C 69.90, H 6.33, N 16.30, S 7.46; found C 69.88, H 6.38, N 16.13, S 7.54%.

Electrochemical measurements: Electrochemical measurements were performed with a computer-controlled EG&G PAR 273 potentiostat. The platinum working electrodes were platinum wires sealed in a glass tube with a surface of $A = 0.785$ mm^2 (∅ 1 mm) and were polished down to 0.5 μm (Bühler or Winter polishing paste) prior to use in order to get reproducible surface. The counter electrode consisted of a platinum wire, the reference electrode was a Ag/AgCl secondary electrode. Dichlormethane (Uvasol, Merck) was refluxed and distilled over P_4O_{10} under argon and directly transfered through syringes to the electrochemical cell. Acetonitrile (Licrosolv, Merck) was filtered through aluminium oxide directly into the electrochemical cell. Benzonitrile was distilled prior to use. Tetrabutylammonium hexafluorophosphate puriss. ($Bu_4N^+PF_6^-$) was obtained from Fluka and dried in vacuo at 200 °C.

General procedure for the characterization: A solution of 0.1M $Bu_4N^+PF_6^-$ in CH_2Cl_2 or PhCN or CH_3CN was deoxygenated with dry argon for 15 min. The corresponding compounds were characterized at a concentration of 1×10^{-3} mol l^{-1} using a scan rate of 100 mV s^{-1}.

0947-6539/00/0614-2630 $ 17.50+.50/0 *Chem. Eur. J.* **2000**, *6*, No. 14

Spectroelectrochemical measurements: UV/Vis spectra were recorded on a Perkin–Elmer spectrophotometer Lambda 19, EG&G PAR potentiostat, model 363, was used. All optical measurements were carried out in a thin-layer electrochemical cell (distance working electrode/light conductor: 60 μm) according to Salbeck[16] incorporating a polished platinum electrode (∅ 6 mm) as the working electrode, an Ag/AgCl wire as the reference electrode and a platinum sheet as the counter electrode. Spectra were recorded in a reflection modus at the platinum electrode with the aid of a *y*-type optical fibre bundle. The preparation of the working electrode for optical measurements was performed in the same way as described for the preparation of working electrodes used in the electrochemical investigations.

ESR and ENDOR measurements: All samples were prepared under high vacuum in Pyrex tubes. CH_2Cl_2 was refluxed and kept over molecular sieves, under high vacuum. 1,1,1,3,3,3-Hexafluoropropanol was purchased from Merck and used without further purification. The following oxidants were used: $AlCl_3$, $SbCl_3$ (sublimed under high vacuum), $AgClO_3$, $Tl(CF_3COO)_3$, $Hg(CF_3COO)_2$ (dried under high vacuum), and tris(*p*-bromophenyl)ammoniumyl hexachloroantimonate.

ESR spectra were measured either with a Varian E9 (attached to a data processing system, Walther AG, Zürich, Switzerland), or a Bruker ESP 300-X band spectrometer. The latter instrument also served for the use multiple-resonance techniques (ENDOR, TRIPLE). Both instruments were equipped with variable-temperature units. The SEOS spectra were recorded a TIDAS diode-array optical fiver spectrometer (J&M, Aalen, Germany) attached to an optical ESO cavity (on a Varian E9).

Single crystal X-ray structure determination: Compound **1** is crystallized with one molecule of the solvent. Details of data collection, structure solution and refinement for $\mathbf{1}_{\mathbf{RED}}$,[17] $\mathbf{2}_{\mathbf{RED}}$,[17] and $\mathbf{3}_{\mathbf{RED}}$[17] are given in Table 6.

Computational procedures

A) ab initio Calculations and structure of the radicals $\mathbf{1}-\mathbf{3}_{\mathbf{SEM}}^{\bullet+}$: The ESR spectra described above show a limited resolution. On the other hand, application of the ENDOR technique reveals well defined ^{1}H hfcs. However, a clear-cut assignment of these hfcs is not possible because the broad ESR lines impede to establish the multiplicities (or number of nuclei) conected with the individual hfcs.

The recent time it has been shown that application of quantum chemical calculations on the density-functional level of theory allow a rather precise prediction of hfcs in organic radicals.[18, 19] Therefore, to establish the structure of radicals $\mathbf{1}^{\bullet+}-\mathbf{3}^{\bullet+}$ and to calculate the hfcs, we have optimized their geometry by ab initio calculations on the UHF/3-21G* level of theory and determined the hfcs by the UB3LYP/6-31G* procedure.[20–22] Trial calculations indicate that in $\mathbf{1}^{\bullet+}-\mathbf{3}^{\bullet+}$, several rotamers have comparable energies. Thus, we have restricted the symmetry to $C_i^{\bullet}$ in the UHF calculations. This restriction allows a variety of planar and non-planar conformations but avoids the occurence of too many unsymmetrical structures. The ESR/ENDOR spectra reflex a rather high symmetry of the radical cations mirrored by the low numbers of different hfcs. Quantum

Table 6. Crystal data, data collection, structure solution, and refinement parameters for compounds $\mathbf{1}\cdot C_6H_5CH_3$, **2**, and **3**.

	$\mathbf{1}\cdot C_6H_5CH_3$	**2**	**3**
Crystallographic section			
Empirical formula	$C_{34}H_{40}N_4\cdot C_7H_8$	$C_{36}H_{42}N_4$	$C_{34}H_{40}N_6$
Molecular mass	596.72	530.76	532.73
a [pm]	1397.3(2)	633.21(8)	1001.25(6)
b [pm]	1210.2(1)	1151.2(2)	1358.46(7)
c [pm]	1926.1(2)	1181.7(2)	1157.65(9)
α [deg]		115.943(9)	
β [deg]	90.09(1)	95.67(1)	100.335(6)
γ [deg]		98.17(1)	
V [pm^3]	$3257.2(6)\times10^6$	$754.1(2)\times10^6$	$1549.0(2)\times10^6$
Z	4	1	2
ρ(calcd) [g cm^{-3}]	1.217	1.169	1.142
crystal system	monoclinic	triclinic	monoclinic
space group	$P2_1/n$	$P1$	$P2_1/c$
Data collection			
diffractometer	Bruker AXS P4	Bruker AXS P4	Bruker AXS P4
radiation	$Mo_{K\alpha}$	$Mo_{K\alpha}$	$Mo_{K\alpha}$
monochromator	graphite	graphite	graphite
crystal size [mm]	$0.25\times0.35\times0.65$	$0.05\times0.15\times0.1$	$0.2\times0.4\times0.45$
data collection mode	ω scan	ω scan	ω scan
θ range [deg]	1.75–27.5	1.75– 27.5	1.75– 27.5
Recip. latt. segment	$h=0\rightarrow18$	$h=-1\rightarrow8$	$h=0\rightarrow13$
	$k=0\rightarrow15$	$k=-13\rightarrow13$	$k=-17\rightarrow0$
	$l=-25\rightarrow25$	$l=-15\rightarrow15$	$l=-15\rightarrow14$
no. reflections measured	8140	3958	3881
no. unique reflections	7466	3056	3524
no. reflections $F>3\sigma(F)$	3521	1773	2542
lin. abs. coeff. [mm^{-1}]	0.07	0.07	0.07
abs. correction	ψ scan	ψ scan	ψ scan
Structural analysis and refinement			
solution method	direct phase determination	direct phase determination	direct phase determination
method of refinement	full-matrix LSQ	full-matrix LSQ	full-matrix LSQ
	H positions of riding model with fixed isotropic U	H positions of riding model with fixed isotropic U	H positions of riding model with fixed isotropic U
data-to-parameter ratio	9.49	9.80	14.04
R, R_w	0.107, 0.102	0.091, 0.087	0.069, 0.063
weighting scheme	$w=1/\sigma^2(F)$	$w=1/\sigma^2(F)$	$w=1/\sigma^2(F)$
largest differ. peak [e Å^{-3}]	0.37	0.28	0.31
largest differ. hole [e Å^{-3}]	0.33	0.30	0.38
program used	Siemens SHELXTL PLUS	Siemens SHELXTL PLUS	Siemens SHELXTL PLUS

mechanical calculations were performed with the Gaussian[23] program package. In Figure 8, the calculated hfcs are compared with their experimental counterparts; their agreement is distinct in the case of $\mathbf{1}^{\bullet+}$ and $\mathbf{3}^{\bullet+}$. Not only the ^{1}H hfcs show a reasonable correlation, but also the ^{14}N hfcs are predicted in a rather reliable way; e.g. for $\mathbf{1}^{\bullet+}$, showing a well resolved ESR signal, and, therefore, allowing a direct determination of the ^{14}N hfcs the agreement is convincing: The predicted ^{14}N hfc of 0.14 mT, attributed to the four equivalent dimethylamino nitrogen atoms, is nearly matched by the experimentally established value of 0.152 mT. A similar agreement holds for the remaining hyperfine data of $\mathbf{2}_{\mathbf{SEM}}{}^{\bullet+}$ and $\mathbf{3}_{\mathbf{SEM}}{}^{\bullet+}$ can be pursued. Using the calculated proton hfcs for the assignment and, coincidentally, for the determination of the corresponding signal multiplicities of the ENDOR data and using values close to the calculated ^{14}N hfcs, a good fit of the ESR signals widths is achieved in the case of $\mathbf{2}_{\mathbf{SEM}}{}^{\bullet+}$ (Figure 8).

B) Semiempirical calculations: The geometries of compounds **1**–**4** were optimized using the MNDO-PM3 semiempirical method as implemented in the HyperChem 5.02 package of programs.[24] Polak–Ribiere algorithm was used for the optimization with SCF convergence limit of 1×10^{-5}; the gradient norm achieved in all the calculations was less than 0.005 kcal mol^{-1} Å^{-1}. Restricted Hartree–Fock (RHF) formalism was used for neutral molecules (RED), dications (OX^{2+}), and tetracations (OX^{4+}), whereas spin-unrestricted Hartree–Fock (UHF) formalism was used for radical cations ($SEM^{\bullet+}$) and radical trications ($SEM^{\bullet+3}$). As the phenyl rings in some oxidation states are not exactly planar, the dihedral angles γ_A, γ_B, γ_C, γ_D between the phenyls planes and the plane of central C–C bond (for **1**), C-C-C-C or C-N-N-C fragments (for **2** or **3**,**4**) were defined as corresponding torsion angles, for example for **1** γ_A = C20-C15-C2-C1 or C16-C15-C2-C1, which is lower and these values are tabulated in Tables 2–5. The signs of rotations are omitted in the Tables for both PM3 calculated geometries and single crystal X-ray structures of **1**–**4**.

Acknowledgement

Financial support by Volkswagen-Stiftung, BASF AG/Ludwigshafen (BMFT project 03 M 4067 6) and Fonds der Chemischen Industrie is highly acknowledged. I.F.P. thanks Alexander von Humboldt Stiftung for a postdoctoral fellowship (1995-97) to conduct some of his research work in Würzburg.

[1] Part LXVII: See ref. [2].
[2] Part 1: S. Hünig, M. Kemmer, H. Wenner, I. F. Perepichka, P. Bäuerle, A. Emge, G. Gescheidt, *Chem. Eur. J.* **1999**, *5*, 1969–1973.
[3] I. F. Perepichka, Alexander von Humboldt Fellow, 9/1995 to 3/1997 (University of Würzburg).
[4] a) S. Hünig, *Chimia* **1978**, *32*, 91–93; b) K. Deuchert, S. Hünig, *Angew. Chem.* **1978**, *90*, 927–938; *Angew. Chem. Int. Ed. Engl.* **1978**, *17*, 875–886; c) S. Hünig, H. Berneth, *Top. Curr. Chem.* **1980**, *92*, 1–44; d) For a theoretical comparison of violenes and cyanines see: S. F. Nelson, H. Q. Trans, M. A. Nagy, *J. Am. Chem. Soc.* **1998**, *120*, 298–304.
[5] R. Willstätter, M. Goldmann, *Ber. Dtsch. Chem. Ges.* **1906**, *39*, 3765–3776.
[6] a) R. Wizinger, *Ber. Dtsch. Chem. Ges.* **1927**, *60*, 1377–1389; b) D. H. Anderson, R. M. Elofson, H. S. Gutowsky, S. Levine, R. B. Sandlin, *J. Am. Chem. Soc.* **1961**, *83*, 5157; c) R. M. Elofson, D. H. Anderson, H. S. Gutowsky, R. S. Sandlin, K. F. Schulz, *J. Am. Chem. Soc.* **1963**, *85*, 2622–2624.
[7] a) A. J. Bard, J. Phelps, *J. Electroanal. Chem.* **1970**, *25*, App. 2; b) J. Phelps, A. J. Bard, *Electroanal. Chem.* **1976**, *68*, 313–335.
[8] G. Gescheidt, *Rev. Sci. Instrum.* **1994**, *65*, 2145.
[9] S. Hünig, H. Quast, *Optische Anregung organischer Systeme*, *II. Intern. Farbensymposium 1964* (Ed. W. Foerst), Verlag Chemie, **1966**, 184–262.
[10] CompareH. Kahn, *Helv. Chim. Acta* **1951**, *34*, 2371–2378.
[11] H. Bock, K. Ruppert, K. Merzweiler, D. Fenske, G. Goesmann, *Angew. Chem.* **1989**, *101*, 1715–1717; *Angew. Chem. Int. Ed. Engl.* **1989**, *28*, 1685–1687.
[12] See literature cited in ref. [11].
[13] W. Tadros, *J. Chem. Soc.* **1954**, 2966–2968.
[14] P. Simon, M. Landl, M. Breza, *Dyes Pigm.* **1999**, *43*, 227–233.
[15] H. H. Szmanet, C. McGinnis, *J. Am. Chem. Soc.* **1950**, *72*, 2890–2892.
[16] J. Salbeck, *J. Electroanal. Chem.* **1992**, *340*, 169–195.
[17] Crystallographic data (excluding structure factors) for the structure reported in this paper have been deposited with the Cambridge Crystallographic Data Centre as supplementary publication no. CCDC-127523 ($\mathbf{1}_{\mathbf{RED}}$), -127524 ($\mathbf{2}_{\mathbf{RED}}$) and -127525 ($\mathbf{3}_{\mathbf{RED}}$). Copies of the data can be obtained free of charge on application to CCDC, 12 Union Road, Cambridge CB21EZ, UK (fax: (+44) 1223-336-033; e-mail: deposit@ccdc.cam.ac.uk).
[18] R. Batra, B. Giese, M. Spichty, G. Gescheidt, K. N. Houk, *J. Phys. Chem.* **1996**, *100*, 18371–18379.
[19] J. W. Gauld, L. A. Eriksson, L. Radom, *J. Phys. Chem.* **1997**, *101*, 1352–1359.
[20] A. D. Becke, *Phys. Rev. A* **1988**, *38*, 3098–3100.
[21] A. D. Becke, *J. Chem. Phys.* **1993**, *98*, 1372–1377.
[22] C. Lee, W. Yang, R. G. Parr, *Phys. Rev. B* **1988**, *37*, 785–789.
[23] M. J. Frisch, G. W. Trucks, H. B. Schlegel, P. M. W. Gill, B. G. Johnson, M. A. Robb, J. R. Cheeseman, T. Keith, G. A. Petersson, J. A. Montgomery, K. Raghavachari, M. A. Al-Laham, V. G. Zakrzewski, J. V. Ortiz, J. B. Foresman, J. Cioslowski, B. B. Stefanov, A. Nanayakkara, M. Challacombe, C. Y. Peng, P. Y. Ayala, W. Chen, M. W. Wong, J. L. Andres, E. S. Replogle, R. Gomperts, R. L. Martin, D. J. Fox, J. S. Binkley, D. J. Defrees, J. Bake, J. P. Stewart, M. Head-Gordon, C. Gonzales, J. A. Pople, *Gaussian 94*, *Revision B.2*, Pittsburgh PA, **1995**.
[24] HyperChem, Release 5.02 for Windows95/NT, **1997**, Molecular Modelling System, Hypercube Inc., Gainesville, Florida, USA.

Received: December 22, 1999 [F2202]

  0947-6539/00/0614-2632 $ 17.50+.50/0